

A semi-analytic model of pairwise velocity distribution between dark matter halos

MASATO SHIRASAKI,^{1,2} ERIC M. HUFF,³ KATARINA MARKOVIC,³ AND JASON D. RHODES^{3,4}

¹*National Astronomical Observatory of Japan, Mitaka, Tokyo 181-8588, Japan*

²*The Institute of Statistical Mathematics, Tachikawa, Tokyo 190-8562, Japan*

³*Jet Propulsion Laboratory, California Institute of Technology, 4800 Oak Grove Drive, Pasadena, CA, USA*

⁴*Kavli Institute for the Physics and Mathematics of the Universe (WPI), The University of Tokyo Institutes for Advanced Study (UTIAS), The University of Tokyo, Chiba 277-8583, Japan*

Submitted to ApJ

ABSTRACT

We study the probability distribution function (PDF) of relative velocity between two different dark matter halos (i.e. pairwise velocity) with high-resolution cosmological N -body simulations. We revisit a non-Gaussian framework to predict pairwise velocity statistics developed in Tinker (2007). We investigate the pairwise velocity PDFs over a wide range of halo masses of $10^{12.5} \lesssim M [h^{-1}M_{\odot}] \lesssim 10^{15}$ and redshifts of $0 < z < 1$. At a given set of masses, redshift and the separation length between two halos, our model requires three parameters to set the pairwise velocity PDF, whereas previous non-Gaussian models in the literature assume four or more free parameters. At the length scales of $5 < r [h^{-1}\text{Mpc}] < 40$, our model predicts the mean and dispersion of the pairwise velocity for dark matter halos with their masses of $10^{12.5} \lesssim M [h^{-1}M_{\odot}] \lesssim 10^{13.5}$ at $0.3 < z < 1$ with a 5%-level precision. We demonstrate that our model of the pairwise velocity PDF provides an accurate mapping of the two-point clustering of massive-galaxy-sized halos at the scales of $O(10) h^{-1}\text{Mpc}$ between redshift and real space for a given real-space correlation function. For a mass-limited halo sample with their masses greater than $10^{13.5} h^{-1}M_{\odot}$ at $z = 0.55$, our model can explain the monopole and quadrupole moments of the redshift-space two-point correlations with a precision better than 5% at the scales of $5 - 40$ and $10 - 30 h^{-1}\text{Mpc}$, respectively. Our model of the pairwise velocity PDF will give a detailed explanation of statistics of massive galaxies at the intermediate scales in redshift surveys.

Keywords: cosmology: large-scale structure of universe — galaxies: halos — methods: numerical

1. INTRODUCTION

Accelerating expansion of the late-time Universe is a long-standing mystery in modern astronomy (e.g. Weinberg et al. 2013, for a review about observational probes). There are two leading physical models to solve the most surprising cosmological discovery in many decades. One is the dark energy model which assumes an exotic form of energy in the Universe, and the other requires a modification of General Relativity at long-length and weak-force regimes. To distinguish the two models in an observational way, one needs detailed measurements of cosmic mass density and velocity over a large volume in the Universe. A modification of gravity can induce the scale dependence on the gravitational growth and flow of cosmic mass density even at linear scales, while the large-scale density growth and flow can be uniquely determined by the expansion rate of the Universe alone in the presence of a smooth uniform dark energy under General Relativity (but see, e.g. Jain & Zhang 2008, for more detailed discussions).

Among observational probes, redshift surveys of distant galaxies are one of the most promising approaches to investigating density and velocity fields. In the standard theory of formation of large-scale structures, galaxies are thought to be a tracer of underlying cosmic mass density. Their clustering properties contain rich cosmological

information in principle. The main challenges to use galaxies for cosmological studies are that galaxies are a biased tracer of density fields and a galaxy bias may depend on various factors. Throughout this paper, we consider a halo-based model for the galaxy bias. Dark matter halos are gravitationally-bounded objects formed in cosmic matter distributions and a building block of large-scale structures (see, [Cooray & Sheth 2002](#), for a review of the halo model). In the halo model, one commonly assumes that dark matter halos host some galaxies and the number of galaxies in single halos depends on the halo mass alone. These assumptions enable us to explain the observed clustering of a variety of galaxies in a precise way (e.g. [Zehavi et al. 2005](#); [Cooray 2006](#); [Zehavi et al. 2011](#)). Nevertheless, the common halo-galaxy connection may cause serious systematic errors in galaxy-based cosmological analyses if the galaxy bias depends on other properties (e.g. [Croton et al. 2007](#); [Zentner et al. 2014](#)).

The two-point correlation function ξ_{gg} is a common observable in galaxy redshift surveys to measure the clustering of galaxies. In a universe with statistical isotropy, the two-point correlation depends on the separation length between galaxies alone. However, actual surveys rely on the observation of redshifts to infer the line-of-sight distances to individual galaxies. A redshift z in the spectrum of each galaxy is caused by cosmic expansion as well as the peculiar velocity of the galaxy itself. Hence, the spatial coordinate inferred by the observation of redshifts is different from the true counterpart. This effect is known as redshift-space distortions and the observed spatial separation (i.e. in redshift space) for a given pair of galaxies is then expressed as

$$s_p = r_p, \quad (1)$$

$$s_\pi = r_\pi + \frac{(1+z)v_z}{H(z)}, \quad (2)$$

where $H(z)$ is the Hubble parameter at z , r_p and r_π represents the perpendicular and parallel components with respect to the line-of-sight direction, s_p and s_π are the counterparts in redshift space, and v_z is the relative velocity between two galaxies (i.e. the pairwise velocity) along the line of sight. In redshift space, the line of sight toward each galaxy is a special direction and the observed two point correlation function depends on both of s_p and s_π . The relation of the two-point correlation between real and redshift space is given by (e.g. [Peebles 1980](#); [Scoccimarro 2004](#)),

$$1 + \xi_{\text{gg}}^S(s_p, s_\pi) = \int_{-\infty}^{\infty} \frac{H(z) dr_\pi}{(1+z)} \mathcal{P}_g \left(v_z = \frac{H(z)(s_\pi - r_\pi)}{(1+z)} \mid s_p, r_\pi \right) \left[1 + \xi_{\text{gg}}(\sqrt{s_p^2 + r_\pi^2}) \right], \quad (3)$$

where \mathcal{P}_g is the probability distribution function (PDF) of the line-of-sight pairwise velocity of galaxies, and ξ_{gg}^S is the two-point correlation function in redshift space. Therefore, it is essential to develop an accurate theoretical model of the pairwise velocity statistics as well as the real-space correlation function for cosmological analyses with redshift surveys.

Measurements of small-scale streaming motions of galaxies may bring meaningful information to improve our understanding of the halo-galaxy relationship. [Xu & Zheng \(2018\)](#) have shown that the dispersion of the pairwise velocity between two dark matter halos depends on properties other than the halo mass, while a similar effect has been found in a semi-analytic galaxy formation model ([Padilla et al. 2019](#)). Apart from the halo-galaxy relationship, numerical simulations have shown that a modification of gravity can change the streaming motion between two massive-galaxy-sized halos with a separation length of $\sim 1 - 5$ Mpc ([Hellwing et al. 2014](#)) as well as the infall velocity of galaxies to massive clusters ([Lam et al. 2012](#); [Zu et al. 2014](#)). To infer the streaming motion of galaxies from observables in galaxy redshift surveys, we require a detailed modeling of the pairwise velocity statistics (e.g. [Scoccimarro 2004](#), also see Eq. 3). Furthermore, measurements of the secondary anisotropy of cosmic microwave background caused by the bulk motion of tracers of large-scale structures, referred to as the kinematic Sunyaev-Zel'dovich effect, have a great potential as a direct probe of the streaming motion of dark matter halos with upcoming experiments (e.g. [Sugiyama et al. 2017, 2018](#); [Smith et al. 2018](#)). Therefore, it is timely and important to develop an accurate model of the pairwise velocity statistics of dark matter halos.

In this paper, we develop a semi-analytic model of the pairwise velocity distribution of dark matter halos with different masses, redshifts, and separations. We pay a special attention to massive-galaxy-sized dark matter halos in this paper. This is because the precise measurements of small-scale two-point clustering are already available (e.g. [Reid et al. 2014](#); [Guo et al. 2015](#)) and the statistical detections of the kinematic Sunyaev-Zel'dovich effect have been reported (e.g. [Hand et al. 2012](#); [De Bernardis et al. 2017](#); [Sugiyama et al. 2018](#)). Using the latest cosmological N -body simulations, we calibrate a physically-intuitive and efficient model of the pairwise velocity developed by [Tinker](#)

(2007) over a range of halo masses $10^{12.5} < M [h^{-1} M_{\odot}] < 10^{15}$ at $0 < z < 1$. We then validate that our model can reproduce the two-point correlation function in redshift space including the non-linear distortion effects due to the peculiar velocity of galaxies. We also study information contents of the pairwise velocity statistics in galaxy clustering analyses.

The paper is organized as follows. In Section 2, we present an overview of the Tinker model and introduce our revised model. In Section 3, we describe the N -body simulations, mock galaxy catalogs, and clustering statistics used in this paper. We summarize our calibration process of the model parameters based on three non-zero moments in the pairwise velocity in Section 4. The results are presented in Section 5 and we mention the limitations in our model in Section 6. Finally, the conclusions and discussions are provided in Section 7.

2. PAIRWISE VELOCITY DISTRIBUTION OF DARK MATTER HALOS

In this section, we briefly introduce a theoretical framework to predict the pairwise velocity statistics of dark matter halos proposed in Tinker (2007). We then present our new model with some modifications. Table 1 summarizes the model parameters in the framework and those are dependent on halo masses, redshifts, and separation lengths.

2.1. Setup

Consider a pair of two halos with their masses of M_1 and M_2 at a given redshift z . The pairwise velocity for the halo pair is then defined as the relative velocity between the two halos,

$$\mathbf{v}_{12}(\mathbf{r}) \equiv \mathbf{v}_1(\mathbf{r}_1) - \mathbf{v}_2(\mathbf{r}_2), \quad (4)$$

where \mathbf{v}_i and \mathbf{r}_i represent the velocity and position of the i -th halo ($i = 1, 2$), and $\mathbf{r} \equiv \mathbf{r}_1 - \mathbf{r}_2$. Throughout this paper, we define the position of a given halo in the comoving coordinate, while the velocity is defined in the physical coordinate. Assuming a spherically symmetric phase-space distribution of halos, we simplify $\mathbf{v}_{12}(\mathbf{r}) = \mathbf{v}_{12}(r)$ where $r = |\mathbf{r}|$. In this paper, we seek a physically-motivated and efficient model of the probability distribution function (PDF) of the pairwise velocity. In particular, we study the dependence of the pairwise velocity PDF on halo masses (M_1 and M_2), redshifts z and the separation length r . Since the line-of-sight component of the pairwise velocity is relevant to statistical analyses in redshift surveys in practice (also see Section 3.3), we focus on two different components in the three-dimensional velocity \mathbf{v} . One is the radial component of v_r and another is the half of the tangential components v_t at each radius r . We define these two components as

$$v_r \equiv \mathbf{v}_{12} \cdot \mathbf{r}/r, \quad (5)$$

$$v_t \equiv v_x \cos \theta \cos \phi + v_y \cos \theta \sin \phi - v_z \sin \theta, \quad (6)$$

where we set a Cartesian coordinate system of $\mathbf{r}/r = (\sin \theta \cos \phi, \sin \theta \sin \phi, \cos \theta)$, the angle θ is defined by the opening angle between the line-of-sight direction and the vector \mathbf{r} , v_x represents the x -axis component of \mathbf{v} in the Cartesian coordinate and so on. Note that v_z corresponds to the line-of-sight velocity in this notation and it holds $v_z = v_r \cos \theta - v_t \sin \theta$.

2.2. The Tinker model

Tinker (2007) proposed an analytic model of the joint PDF of $\mathcal{P}(v_r, v_t | r, M_1, M_2, z)$ for a pair of dark matter halos by assuming the following conditions:

- (i) There exists a latent variable to make the joint PDF non-Gaussian, but the PDF at a given latent variable can be approximated as Gaussian.
- (ii) At a given latent variable, v_r and v_t are assumed to be independent.
- (iii) The latent variable for modeling of $\mathcal{P}(v_r, v_t | r, M_1, M_2, z)$ is set to the local environmental mass overdensity δ around a pair of halos.

These conditions allow us to express the joint PDF as the following functional form:

$$\mathcal{P}(v_r, v_t | r, M_1, M_2, z) = \int d\delta \mathcal{N}(v_t | \mu_t(\delta), \Sigma_t(\delta)) \mathcal{N}(v_r | \mu_r(\delta), \Sigma_r(\delta)) \mathcal{F}(\delta | r, M_1, M_2, z), \quad (7)$$

where $\mathcal{N}(u|\mu, \Sigma)$ represents a Gaussian PDF of a one-dimensional random field u with the mean of μ and the variance of Σ^2 and $\mathcal{F}(\delta|r, M_1, M_2, z)$ is the conditional PDF of the mass over-density field δ when one finds the halo pair with their masses of M_1 and M_2 at the redshift z within the radius of r . In Eq. (7), Tinker (2007) sets the mean v_t at a given δ to be zero ($\mu_t = 0$), while the variables of Σ_t , μ_r , and Σ_r can depend on the halo masses, redshift and radius as well as the environmental density δ . In the following, we summarize key ingredients in Eq. (7).

2.2.1. Conditional PDF of mass overdensity

The unconditional PDF of smoothed mass density at a smoothing scale of r can be described by a log-normal distribution (e.g. Coles & Jones 1991; Kofman et al. 1994; Kayo et al. 2001), while Tinker (2007) found the conditional PDF \mathcal{F} in numerical simulations is well fitted by

$$\mathcal{F}(\delta|r, M_1, M_2, z) = \mathcal{A} \exp\left[-\frac{\tilde{\rho}_0(r, M_1, M_2, z)}{1+\delta}\right] P_{\text{ln}}(\delta|r), \quad (8)$$

where \mathcal{A} is a normalization constant so that $\int d\delta \mathcal{F} = 1$, $\tilde{\rho}_0$ is a density cutoff scale to be calibrated with N -body simulations, and P_{ln} is the log-normal distribution given by

$$P_{\text{ln}}(\delta|r) = \frac{1}{\sqrt{2\pi}\sigma_{\text{ln}}} \exp\left[-\frac{\{\ln(1+\delta) + \sigma_{\text{ln}}^2/2\}^2}{2\sigma_{\text{ln}}^2}\right] \frac{1}{1+\delta}. \quad (9)$$

In Eq. (9), the variance σ_{ln}^2 is set to be $\sigma_{\text{ln}}^2(r, z) = \ln(1 + \sigma_{\text{NL}}^2(r, z))$ where $\sigma_{\text{NL}}^2(r, z)$ is the non-linear mass variance smoothed by a top-hat filter at the scale of r at the redshift z . To be specific, the top-hat mass variance is given by

$$\sigma_{\text{NL}}^2(r, z) = \int_0^\infty \frac{4\pi k^2 dk}{(2\pi)^3} W_{\text{TH}}^2(kr) P_{\text{NL}}(k, z), \quad (10)$$

$$W_{\text{TH}}(x) = \frac{3(\sin x - x \cos x)}{x^3}, \quad (11)$$

where $P_{\text{NL}}(k, z)$ is the non-linear matter power spectrum at z . Tinker (2007) assumed that the density cutoff scale $\tilde{\rho}_0$ takes the form

$$\tilde{\rho}_0(r, M_1, M_2, z) = \tilde{\rho}_1 (b_{\text{L}}(M_1, z) + b_{\text{L}}(M_2, z)) + \left(\frac{r}{r_0}\right)^\alpha, \quad (12)$$

where $b_{\text{L}}(M, z)$ is the linear halo bias at the redshift z , and three parameters of $\tilde{\rho}_1$, r_0 , and α have been calibrated with a set of N -body simulations. Tinker (2007) found the simulation results can be explained by the form of Eq. (8) when $\tilde{\rho}_1 = 1.41$, $\alpha = -2.2$, and $r_0 = 9.4 \times \text{MAX}(R_{200\text{b},1}, R_{200\text{b},2})$ where $R_{200\text{b},i}$ represents a spherical over-density radius of the halo of M_i . We here define the halo mass by $M \equiv M_{200\text{b}} = (4\pi/3) 200\bar{\rho}_{\text{m}0} R_{200\text{b}}^3$, where $\bar{\rho}_{\text{m}0}$ is the mean cosmic mass density today and the halo radius $R_{200\text{b}}$ is defined in the comoving coordinate.

Throughout this paper, we adopt the linear halo bias model in Tinker et al. (2010), while we compute the non-linear matter power spectrum by using the fitting formula calibrated by a set of N -body simulations (Takahashi et al. 2012). Note that we use the linear matter power spectrum *without* the baryon acoustic oscillations (Eisenstein & Hu 1998) when computing σ_{NL}^2 to avoid any oscillations in the predicted velocity moments at large scales of $\gtrsim 10 h^{-1}$ Mpc.

2.2.2. Mean and variance at a given environmental density

For a given halo pair at the separation of r and the environmental density δ , Tinker (2007) developed a model of the mean infall velocity $\mu_r(\delta, r)$ by combining linear theory and the spherical collapse model. The linear theory predicts the relation of the velocity and overdensity fields as

$$\mu_{\text{lin}}(\delta, r, z) = -\frac{H(z)}{1+z} r f(z) \frac{\delta}{3}, \quad (13)$$

where $H(z)$ is the Hubble parameter at z , $f(z) = d \ln D / d \ln(1+z)^{-1}$ where $D(z)$ is the linear growth factor at z^1 . At non-linear scales, the spherical collapse model can provide a reasonable approximation of the mean infall velocity. In the Einstein-de Sitter universe, one can derive the relation of the velocity and density perturbations as

$$\mu_{\text{sc}}(\delta, r, z) = \frac{H(z)}{1+z} r f(z) \mathcal{G}(\delta), \quad (14)$$

¹ We normalize $D(z) = 1$ at $z = 0$ throughout this paper.

where $\mathcal{G}(\delta)$ is expressed in a parametric form as²

$$\delta = \frac{9}{2} \frac{(\gamma - \sin \gamma)^2}{(1 - \cos \gamma)^3} - 1, \quad \mathcal{G} = \frac{3}{2} \frac{\sin \gamma (\gamma - \sin \gamma)}{(1 - \cos \gamma)^2} - 1. \quad (15)$$

Tinker (2007) then proposed a model by combining Eqs. (13) and (14):

$$\mu_r(\delta, r, M_1, M_2, z) = \begin{cases} w(r) \mu_{\text{sc}}(\delta, r, z) \exp \left[- \left(\frac{4.5}{r(1+\delta)} \right)^2 \right] + [1 - w(r)] \mu_{\text{lin}}(\delta, r, z) & (r > R_{\text{cut}}) \\ \mu_{\text{sc}}(\delta_{\text{cut}}, r, z) \exp \left[- \left(\frac{4.5}{r(1+\delta_{\text{cut}})} \right)^2 \right] & (r \leq R_{\text{cut}}) \end{cases}, \quad (16)$$

where $R_{\text{cut}} = \text{MAX}(R_{200\text{b},1}, R_{200\text{b},2})$, $1 + \delta_{\text{cut}} = \exp(-\sigma_{\text{lin}}^2/2)$, and the weight function $w(r)$ and the exponential cutoff have been calibrated against the numerical simulations. Tinker (2007) found that the following weight function shows a reasonable fit to the simulation results,

$$w(r) = \begin{cases} 1 & (r [h^{-1}\text{Mpc}] \leq 4) \\ 1.86 - 0.62 \ln r & (4 < r [h^{-1}\text{Mpc}] \leq 20) \\ 0 & (20 < r [h^{-1}\text{Mpc}]) \end{cases}. \quad (17)$$

For the velocity dispersions $\Sigma_{t,r}$, Tinker (2007) introduced the following parametric form of

$$\Sigma_{t,r} = 200 \text{ [km/s]} \left(\frac{\Omega_{\text{m}}(z)}{0.3} \right)^{0.6} \left(\frac{D(z) \sigma_8}{0.8} \right) \left(\frac{1 + \delta}{\tilde{\rho}_{t,r}} \right)^\beta, \quad (18)$$

where $\Omega_{\text{m}}(z) = \Omega_{\text{m}0}(1+z)^3 / [\Omega_{\text{m}0}(1+z)^3 + (1 - \Omega_{\text{m}0})]$ ($\Omega_{\text{m}0}$ is the mass-density parameter today), σ_8 is the mass variance for the linear overdensity field at $z = 0$ when smoothed by the top-hat filter at $8 h^{-1}\text{Mpc}$, and three parameters $\tilde{\rho}_{t,r}$ and β have been calibrated with the simulation results as a function of r , M_1 and M_2 . Note that the scaling with $\Omega_{\text{m}}(z)$ and σ_8 in Eq. (18) is motivated by the linear theory (recall $f \simeq \Omega_{\text{m}}^{0.6}(z)$). For $M_1 \geq M_2$, the fitting formulas are summarized as

$$\beta(r) = \left(\frac{r}{35 h^{-1}\text{Mpc}} \right)^{0.1}, \quad (19)$$

$$\tilde{\rho}_t(r, M_1, M_2) = \left(\frac{r}{7.2 R_{200\text{b},1}^{1/2}} \right)^{-2.5} + \left(\frac{r}{12.6 R_{200\text{b},0}^{1/2}} \right)^{-0.8} + 0.48, \quad (20)$$

$$\tilde{\rho}_r(r, M_1, M_2) = \left(\frac{r}{5.0 R_{200\text{b},1}^{1/2}} \right)^{-4.0} + \left(\frac{r}{11.5 R_{200\text{b},0}^{1/2}} \right)^{-1.3} + 0.50, \quad (21)$$

where $R_{200\text{b},0} = R_{200\text{b},1} + R_{200\text{b},2}$ in comoving $h^{-1}\text{Mpc}$.

2.3. New model

The model by Tinker (2007) is physically-intuitive and efficient to compute the pairwise velocity PDF for dark matter halos, but we find that it does not provide a reasonable fit to the latest high-resolution simulation results as shown in Section 5. There may be several reasons why the model can not reproduce the simulation results today. A major concern about the model of Tinker (2007) is that its parameter calibration relies on the results of N -body simulations in a ΛCDM cosmology with the spectral index $n_s = 1$ and a larger amplitude of the initial density power spectrum at $k = 0.05 \text{ Mpc}^{-1}$ than the inferred value from Planck (Planck Collaboration et al. 2016). This can affect the kinematics of dark matter halos even at large scales, because the linear velocity in Fourier space scales with δ/k where k is the wave number. In addition, the simulations in Tinker (2007) assume $\Omega_{\text{m}0} = 0.1$ and $\sigma_8 = 0.95$ at $z = 0$, which may result in sizable differences in the non-linear evolution of cosmic mass density. Furthermore, the simulations consist of

² Equation (17) in Tinker (2007) misses the factor of $1/2$ to compute $1 + \mathcal{G}$.

Table 1. A short summary of parameters in the model of pairwise velocity PDF of dark matter halos.

Model parameters	Tinker (2007)	This paper	Reference
$\tilde{\rho}_0$	Eq. (12)	Eq. (22)	Density cutoff scale on the halo formation as in Eq. (8)
μ_r	Eq. (16)	Eq. (23)	Mean radial velocity at a given environmental density
$\tilde{\rho}_{t,r}$	Eqs. (20) & (21)	Eq. (24)	Scale density on the dispersion-density relation as in Eq. (18)

360^3 particles in a volume of $253^3 [h^{-1}\text{Mpc}]^3$ and the mass resolution may be less sufficient to study the halo-galaxy connection in a modern manner. In fact, recent observations of massive galaxies in the Sloan Sky Digital Sky Survey III (SDSS III) have shown that the kinematics of galaxies closely relate to the phase-space density in the inner regions of their host dark matter halos (Reid et al. 2014; Guo et al. 2015), while the halo velocity in Tinker (2007) is defined by the center-of-mass velocity. Detailed simulations show that halo cores are not at rest relative to the halo bulk (Behroozi et al. 2013). High-resolution and large-volume cosmological simulations would be needed to re-calibrate the model of Tinker (2007) and this is the scope of this paper.

Our new model follows the basic concept in Tinker (2007), but we introduce minor revisions so that the final model can reproduce the latest simulation results over a wide range of halo masses, redshifts, and separation lengths. For the conditional PDF of finding a halo pair given a mass density, we adopt the exponential cutoff as in Eq. (8) to effectively include the environmental dependence of halo formation and parametrize the density cutoff scale as in Eq. (12), but we allow a more complicated mass and redshift dependence:

$$\tilde{\rho}_0(r, M_1, M_2, z) = \mathcal{A}_\rho(M_1, M_2, z) (b_L(M_1, z) + b_L(M_2, z)) + \mathcal{B}_\rho(M_1, M_2, z) \left(\frac{r}{\text{MAX}(R_{200b,1}, R_{200b,2})} \right)^{\mathcal{C}_\rho(M_1, M_2, z)} \quad (22)$$

Also, we modify the functional form of mean radial velocity at a given overdensity, $\mu_r(\delta)$, as

$$\mu_r(\delta, r, z) = -\frac{H(z)}{1+z} r \frac{f(z)}{3} \delta_c \left[(1+\delta)^{1/\delta_c} - 1 \right], \quad (23)$$

where $\delta_c = 1.686$. Eq. (23) is the approximate solution of the infall velocity for the spherical collapse model when the initial condition of the radial shells is set by the Zeldovich approximation (Bond & Myers 1996; Shen et al. 2006; Lam & Sheth 2008). Therefore, it naturally reduces to the linear-theory prediction (Eq. [13]) at $\delta \rightarrow 0$ and we do not introduce any weight functions to stitch the solution between non-linear and linear regimes.

For the velocity dispersions, we keep the functional form of Eq (18), but we generalize the dependence of $\tilde{\rho}_{t,r}$ on halo masses and radius by using a double power-law form of

$$\tilde{\rho}_{t,r}(r, M_1, M_2, z) = \mathcal{C}_{t,r}^{(0)}(M_1, M_2, z) r^{p_{t,r}(M_1, M_2, z)} + \mathcal{C}_{t,r}^{(1)}(M_1, M_2, z) r^{q_{t,r}(M_1, M_2, z)} + \mathcal{C}_{t,r}^{(2)}(M_1, M_2, z), \quad (24)$$

where we introduce five functions of $\mathcal{C}^{(i)}$ ($i = 0 - 2$), p and q for each velocity dispersion. Note that the power-law index of Eq. (18) is fixed to Eq. (19) in the new model as well.

The detailed forms of \mathcal{A}_ρ , \mathcal{B}_ρ , \mathcal{C}_ρ , $\mathcal{C}_{t,r}^{(i)}$ ($i = 0 - 2$), $p_{t,r}$, and $q_{t,r}$ are found in Appendix A. We also provide the details of our calibration process to find the forms of various functions in Section 4.

3. DATA

3.1. *N*-body simulations and halo catalogs

To study the pairwise velocity statistics of dark matter halos, we use a set of publicly available halo catalogs provided by the $\nu^2\text{GC}$ collaboration³. Ishiyama et al. (2015) performed a series of high-resolution cosmological (dark-matter-only) *N*-body simulations with various combinations of mass resolutions and volumes on the basis of the ΛCDM cosmology consistent with observational results obtained by the Planck satellite. Among them, we use the halo catalogs based on the largest-volume run called $\nu^2\text{GC-L}$ run, which consists of 8192^3 dark matter particles in a box of $1.12 h^{-1}\text{Gpc}$. The corresponding mass resolution is $2.2 \times 10^8 h^{-1}M_\odot$, allowing us to study the core

³ The data are available at <https://hpc.imit.chiba-u.jp/~mngc/>.

Table 2. The number of dark matter halos analyzed in this paper. Note that the halo mass is defined by the mass of a spherical overdensity, with 200-times the mean density of the universe.

Halo mass	$z = 0$	$z = 0.30$	$z = 0.55$	$z = 1.01$
$10^{12.5} \leq M [h^{-1} M_{\odot}] < 10^{13}$	1,514,560	1,406,363	1,289,149	1,014,952
$10^{13} \leq M [h^{-1} M_{\odot}] < 10^{13.5}$	513,892	444,888	377,278	244,833
$10^{13.5} \leq M [h^{-1} M_{\odot}] < 10^{14}$	155,681	118,600	87,235	40,634
$10^{14} \leq M [h^{-1} M_{\odot}] < 10^{14.5}$	36,977	22,295	12,805	3,339
$10^{14.5} \leq M [h^{-1} M_{\odot}] < 10^{15}$	5,136	2,038	767	68

velocity of dark matter halos in a robust way. The simulations were performed by a massive parallel TreePM code of GreeM³ (Ishiyama et al. 2009, 2012) on the K computer at the RIKEN Advanced Institute for Computational Science, and Aterui super-computer at Center for Computational Astrophysics (CfCA) of National Astronomical Observatory of Japan. The authors generated the initial conditions by a publicly available code, 2LPTic⁴, using second-order Lagrangian perturbation theory (e.g. Crocce et al. 2006), as well as the online version of CAMB⁵ (Lewis et al. 2000) to set the linear power spectrum at the initial redshift of $z = 127$. In the simulations, the following cosmological parameters were adopted: $\Omega_{m0} = 0.31$, $\Omega_{b0} = 0.048$, $\Omega_{\Lambda} = 1 - \Omega_{m0} = 0.69$, $h = 0.68$, $n_s = 0.96$, and $\sigma_8 = 0.83$. These are consistent with Planck (Planck Collaboration et al. 2016).

In this paper, we use the halo catalogs produced with the ROCKSTAR halo finder (Behroozi et al. 2013) at four different redshifts of $z = 0, 0.30, 0.55$ and 1.01 . We focus on parent halos identified by the ROCKSTAR algorithm and exclude any subhalos in the following analyses. The halo position is defined by the center-of-mass location of a subset of member particles in the inner halo density, while the velocity is computed by the average particle velocity within the innermost 10% of the virial radius. We keep the halos with $M > 10^{12.5} h^{-1} M_{\odot}$ as a very conservative choice to study the halo properties (i.e. the smallest halos in the analysis consist of ~ 14000 dark matter particles). To study the mass dependence, we divide the halos into six subgroups by their masses: $M [h^{-1} M_{\odot}] = 10^{12.5-13}$, $10^{13-13.5}$, $10^{13.5-14}$, $10^{14-14.5}$ and $10^{14.5-15}$. Table 2 summarizes the number of dark matter halos in each subgroup of interest. We use these subgroups to calibrate the model parameters as in Section 4.

3.2. Mock galaxy catalogs

To test our model of the pairwise velocity distribution of dark matter halos, we produce a set of mock galaxy catalogs. For the simplest model, we consider a mass-limited sample with the halo mass above M_{th} at different redshifts. For the mass-limited sample, we consider two different mass thresholds of $M_{\text{th}} = 10^{12.5}$ and $10^{13.5} h^{-1} M_{\odot}$, which are typical halo masses of massive early-type galaxies at $z < 1$ (e.g. Zheng et al. 2007, 2009; Reid & Spergel 2009; Leauthaud et al. 2012; Tinker et al. 2017). In the mass-limited sample, we do not include satellite galaxies in their host halos and assume that there exist single galaxies at the center of their hosts. These mass-limited samples enable us to examine our interpolation scheme over the halo masses in the model of the pairwise velocity distribution.

For a more realistic catalog, we employ the halo occupation distribution (HOD) method that allows us to populate hypothetical galaxies into halos in the simulations. The HOD, denoted by $\langle N_{\text{gal}} \rangle_M$, gives the mean number of galaxies in host halos with mass M . As a representative example, we consider the spectroscopic sample of massive galaxies in the SDSS-III Baryon Oscillation Spectroscopic Survey (BOSS). There are two targets of galaxies in the BOSS, but we focus on the sample referred to as CMASS. The CMASS sample is designed to be a roughly volume-limited sample of massive, luminous galaxies (Masters et al. 2011) and has a large galaxy bias of $b \sim 2$, showing that most galaxies reside in the dark matter halos of $M \sim 10^{13} h^{-1} M_{\odot}$ (White et al. 2011).

For the HOD of the CMASS sample, we adopt the model in Reid et al. (2014) with the form of

$$\langle N_{\text{gal}} \rangle_M = \langle N_{\text{cen}} \rangle_M + \langle N_{\text{sat}} \rangle_M, \quad (25)$$

$$\langle N_{\text{cen}} \rangle_M = \frac{1}{2} \left[1 + \text{erf} \left(\frac{\log_{10} M - \log_{10} M_{\text{min}}}{\sigma_{\log_{10} M}} \right) \right], \quad (26)$$

$$\langle N_{\text{sat}} \rangle_M = \langle N_{\text{cen}} \rangle_M \left(\frac{M - M_{\text{cut}}}{M_1} \right)^{\alpha_M} \mathcal{H}(M - M_{\text{cut}}), \quad (27)$$

⁴ <http://cosmo.nyu.edu/roman/2LPT/>

⁵ <http://lambda.gsfc.nasa.gov/toolbox/tbcambform.cfm>

where $\mathcal{H}(x)$ is the Heaviside step function, $\langle N_{\text{cen}} \rangle_M$ and $\langle N_{\text{sat}} \rangle_M$ represent the HODs for the central and the satellite galaxies, respectively. We adopt the best-fit parameters in Reid et al. (2014): $\log_{10} M_{\text{min}} = 13.031$, $\sigma_{\log_{10} M} = 0.38$, $\log_{10} M_{\text{cut}} = 13.27$, $\log_{10} M_1 = 14.08$, and $\alpha_M = 0.76$. Using the HOD in Eqs. (25)-(27), we populate the $\nu^2\text{GC-L}$ halos with hypothetical CMASS galaxies at $z = 0.55$ in the following manner.

- (i) We populate halos with central CMASS galaxies by randomly selecting halos according to the probability distribution, $\langle N_{\text{cen}} \rangle_M$ (Eq. [26]). In this step, we assume that each central galaxy resides at the halo center and is at rest with respect to the host halo.
- (ii) When halos have central galaxies, we then randomly populate the halos with satellite galaxies assuming a Poisson distribution with the mean of $\lambda_M = [(M - M_{\text{cut}})/M_1]^{\alpha_M} \mathcal{H}(M - M_{\text{cut}})$. We assume that the radial distribution of satellites on average follows that of dark matter in each host halo. We simply assume the analytical Navarro-Frenk-White (NFW) profile (Navarro et al. 1996), where we use the concentration-mass-redshift relation in Diemer & Kravtsov (2015), to compute the density profile for each host halo. We set the halo-centric radius of each satellite by drawing a random variable q which follows $M_{\text{NFW}}(< q)/M_{\text{NFW}}(< R_{200b})$. Here $M_{\text{NFW}}(< r)$ represents the enclosed mass predicted by the NFW profile as a function of radius r .
- (iii) For each satellite galaxy, we assign a virial random motion by using a Gaussian random variable with the zero mean and the variance of $\sigma_{\text{vir}}^2 = (1 + z)GM/(2R_{200b})$. Note that the halo radius is defined in the comoving coordinate in this paper.

After adopting the above procedures, we find the number density of our mock galaxies to be $4.37 \times 10^{-4} [(h \text{ Mpc}^{-1})^3]$. This density is in good agreement with the value in Reid et al. (2014)⁶. Note that in principle we could use the concentration of individual halos measured by ROCKSTAR to set the NFW distribution of satellites. Instead we simply adopt the model of Diemer & Kravtsov (2015) to ignore a possible impact of scatter in the halo concentration. Our primary purpose is to validate if our model can be suitable to model the two-point correlation function in redshift space at a scale of $\sim 10 h^{-1} \text{ Mpc}$ where the dominant contribution to any clustering observable is expected to come from pairs of central galaxies (e.g. Zheng & Guo 2016).

3.3. Clustering statistics

For a given catalog of mock galaxies in Section 3.2, we perform a two-point clustering analysis in redshift space to test if our model is useful for the most widely used statistics in redshift surveys. The two-point correlation function of galaxies is formally defined by

$$\langle n_{\text{g}}(\mathbf{r}_1)n_{\text{g}}(\mathbf{r}_2) \rangle = \bar{n}_{\text{g}}^2 (1 + \xi_{\text{gg}}(\mathbf{r})), \quad (28)$$

where $\mathbf{r} = \mathbf{r}_1 - \mathbf{r}_2$, n_{g} represents the number density field of galaxies of interest, \bar{n}_{g} is the mean density, and $\xi_{\text{gg}}(\mathbf{r})$ is the two-point correlation function. Since distances to individual galaxies are affected by the redshift-space distortion, the galaxy two-point correlation must be anisotropic as in Eq. (3) in practice. Eq. (3) also shows that the anisotropy in the observed galaxy clustering is set by the pairwise velocity PDF for a given cosmology. According to this fact, we shall validate our model of pairwise PDFs by studying the mapping of two-point correlation functions between real and redshift space.

In this paper, we measure the two-point correlation functions, ξ_{gg}^S and ξ_{gg} for a given mock catalog. For comparison, we then predict ξ_{gg}^S by using Eq. (3) with the true ξ_{gg} in the simulations and our model of $\mathcal{P}_{\text{g}}(v_z)$. We derive an analytic expression of $\mathcal{P}_{\text{g}}(v_z)$ for the HOD-based model in Appendix B. In the simulations, we adopt the distant-observer approximation. For the line-of-sight direction, we set an axis in the Cartesian coordinate system applied to the simulation box. We measure the two point correlation function by using the natural estimator of $\text{DD}/\text{RR} - 1$ where DD and RR represent the number of pairs of galaxies and random points at a given separation, respectively⁷. In the periodic box without boundaries, we can compute the number of random points analytically. For the measurement of $\xi_{\text{gg}}(r)$, we employ the logarithmic binning in the range of $r = 0.01 h^{-1} \text{ Mpc}$ to $100 h^{-1} \text{ Mpc}$ with the number of bins being

⁶ The difference between two is a 6% level.

⁷ The Landy-Szalay estimator (Landy & Szalay 1993) is often adopted in the literature and has a different form from $\text{DD}/\text{RR} - 1$. However, the difference between two is only important for large scales of $\sim 100 \text{ Mpc}$. Since we are working on smaller scales ($\sim 10 \text{ Mpc}$), it should not be necessary for our purpose.

40. For the redshift-space correlation, we measure $\xi_{\text{gg}}^S(s_p, s_\pi)$ in the linearly-spaced bins over $0 < s_{p,\pi} [h^{-1} \text{ Mpc}] < 50$ with the number of bins in each direction being 50. We measure ξ_{gg}^S while changing three axes in the Cartesian coordinate system. We then take the average over 3 realizations to have final results of ξ_{gg}^S .

In practice, it is more common to compress the information in the two-point correlation in redshift space by using the Legendre expansion:

$$\xi_\ell(s) \equiv \frac{2\ell + 1}{2} \int_{-1}^1 d\mu \xi_{\text{gg}}^S(s_p, s_\pi) \mathcal{L}_\ell(\mu), \quad (29)$$

where $s = (s_p^2 + s_\pi^2)^{1/2}$, $\mu = s_\pi/s$, $\mathcal{L}_\ell(\mu)$ is the Legendre polynomial of order ℓ . We measure the first three non-zero moments ($\ell = 0, 2, 4$) for a given mock catalog. We evaluate $\xi_\ell(s)$ by using the measurement of $\xi_{\text{gg}}^S(s_p, s_\pi)$ with 20 logarithmic bins in the range of $0.5 < s [h^{-1} \text{ Mpc}] < 50.0$ and 40 linear bins of μ with the width of $\Delta\mu = 0.05$. For comparison purposes, we estimate the variance of $\xi_\ell(s)$ by dividing the data volume into 2^3 sub-volumes and measuring $\xi_\ell(s)$ for galaxies in each sub-volume. We then compute the variance of $\xi_\ell(s)$ at a given s as

$$\text{Var}[\xi_\ell(s)] = \frac{V_{\text{sub}}}{V_{\text{full}}} \frac{1}{N-1} \sum_{i=1}^N [\xi_\ell(s; i) - \bar{\xi}_\ell(s)]^2, \quad (30)$$

where $N = 8$, V_{sub} is the sub-volume, V_{full} is the full data volume, $\xi_\ell(s; i)$ represents the clustering multipole for the i -th subsample, and $\bar{\xi}_\ell(s)$ is the average multipole over 8 sub-volumes. Note that $V_{\text{full}} = 8V_{\text{sub}}$. Eq. (30) provides a rough estimate of the sample variance of the measurements of $\xi_\ell(s)$ for the survey volume of $(1.12)^3 \simeq 1.40 [h^{-1} \text{ Gpc}]^3$.

4. CALIBRATION OF THE MODEL PARAMETERS

In this section, we summarize how to calibrate the model parameters in Section 2 with the pairwise velocity statistics in the simulations. In principle, we can determine the functions of $\tilde{\rho}_0(r, M_1, M_2, z)$, $\tilde{\rho}_t(r, M_1, M_2, r)$ and $\tilde{\rho}_r(r, M_1, M_2, r)$ by using the smoothed density distribution from N -body particles and the statistics of halo pairs. Unfortunately, the particle data in the $\nu^2\text{GC-L}$ run are not saved because of the hard drive shortage. Hence, we assume the specific forms of three functions $\tilde{\rho}_0(r, M_1, M_2, z)$, $\tilde{\rho}_t(r, M_1, M_2, r)$ and $\tilde{\rho}_r(r, M_1, M_2, r)$ as in Eqs (22) and (24), but we attempt to find the parameters in the functions so that the model can reproduce the first three non-zero moments of the pairwise velocity in the simulations.

Given the joint PDF in Eq. (7), one can find the first three non-zero moments as

$$\begin{aligned} \langle v_r \rangle(r, M_1, M_2, z) &\equiv \int dv_t dv_r v_r \mathcal{P}(v_t, v_r | r, M_1, M_2, z) \\ &= \int d\delta \mu_r(\delta, r, z) \mathcal{F}(\delta | r, M_1, M_2, z), \end{aligned} \quad (31)$$

$$\begin{aligned} \sigma_t^2(r, M_1, M_2, z) &\equiv \int dv_t dv_r v_t^2 \mathcal{P}(v_t, v_r | r, M_1, M_2, z) \\ &= \int d\delta \Sigma_t^2(\delta, r, M_1, M_2, z) \mathcal{F}(\delta | r, M_1, M_2, z), \end{aligned} \quad (32)$$

$$\begin{aligned} \sigma_r^2(r, M_1, M_2, z) &\equiv \int dv_t dv_r v_r^2 \mathcal{P}(v_t, v_r | r, M_1, M_2, z) - [\langle v_r \rangle(r, M_1, M_2, z)]^2 \\ &= \int d\delta \Sigma_r^2(\delta, r, M_1, M_2, z) \mathcal{F}(\delta | r, M_1, M_2, z) \\ &\quad + \int d\delta \mu_r^2(\delta, r, z) \mathcal{F}(\delta | r, M_1, M_2, z) - [\langle v_r \rangle(r, M_1, M_2, z)]^2, \end{aligned} \quad (33)$$

where $\tilde{\rho}_0(r, M_1, M_2, z)$ sets the functional form of \mathcal{F} , while $\tilde{\rho}_{t,r}(r, M_1, M_2, z)$ is involved in the functions of $\Sigma_{t,r}^2$. Because our model assumes the functional form of μ_r is known as Eq. (23), Eqs (31)-(33) may provide sufficient information to determine the model parameters in $\tilde{\rho}_0$ and $\tilde{\rho}_{t,r}$. In this paper, we first find the parameters in $\tilde{\rho}_0$ (i.e. \mathcal{A}_ρ , \mathcal{B}_ρ , and \mathcal{C}_ρ in Eq. [22]) by the least square fitting of the profile $\langle v_r \rangle(r, M_1, M_2, z)$ for a given set of masses and redshift (M_1, M_2 , and z). After finding the best-fit values of \mathcal{A}_ρ , \mathcal{B}_ρ , and \mathcal{C}_ρ by fitting of $\langle v_r \rangle(r)$, we then find the best-fit parameters in Eq. (24) by comparing the profiles of $\sigma_t^2(r)$ and $\sigma_r^2(r)$ with the predictions as in Eqs (32) and (33).

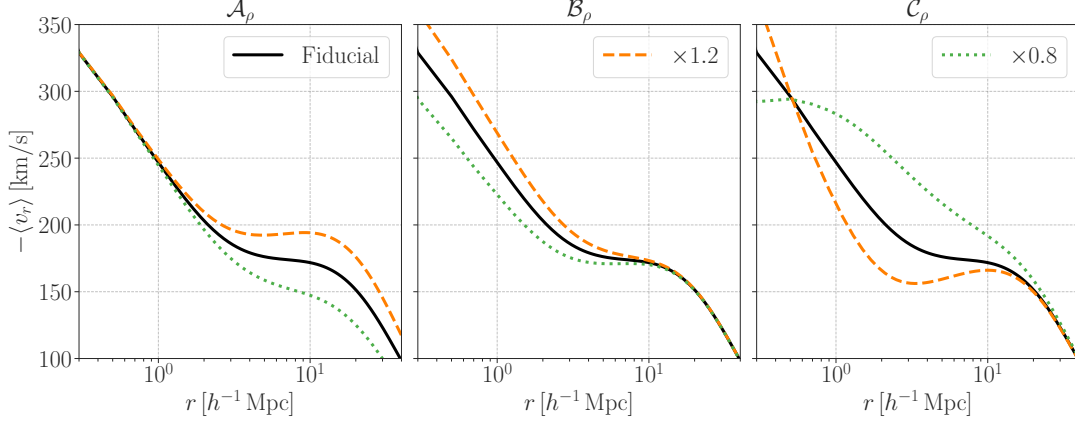


Figure 1. Dependence of the mean radial velocity profile on the model parameters in Section 2. In each panel, the solid line shows the profile when we adopt the parameters proposed in Tinker (2007), while the dashed (dotted) line stand for the cases when varying a given parameter by a factor of 1.2 (0.8). The left, middle, right panels show the dependence on \mathcal{A}_ρ , \mathcal{B}_ρ , and \mathcal{C}_ρ , respectively. In this figure, we consider the halo pairs of $M_1 = M_2 = 10^{13} h^{-1} M_\odot$ at $z = 0$.

Figure 1 shows the model prediction of the mean radial velocity profile as a function of model parameters \mathcal{A}_ρ , \mathcal{B}_ρ , and \mathcal{C}_ρ in Eq. (22). In the figure, we consider a pair of halos with their masses of $M_1 = M_2 = 10^{13} h^{-1} M_\odot$. The figure represents a good flexibility of our model for fitting of $\langle v_r \rangle$. For the velocity dispersions, we fix four parameters in the fitting process to avoid a complex degeneracy among parameters. To be specific, we fix $\mathcal{C}_t^{(2)} = 0.45$, $q_t = -0.9$, $p_r = -4.0$, and $q_r = -1.3$ in this paper. Even if we reduce the number of degree of freedoms, the model prediction is found to be sufficiently flexible to fit the profiles of σ_t^2 and $\sigma_r^2(r)$ in the simulation.

In the fitting processes, we measure the three moments of the pairwise velocity for the samples in Table 2. For the measurements, we employ a linear-space binning in the range of $0 < r [h^{-1} \text{Mpc}] < 40$ with 200 bins. For a given halo sample, we then find the best-fit values of \mathcal{A}_ρ , \mathcal{B}_ρ and \mathcal{C}_ρ in a given M_1 , M_2 , and z bin by minimizing the following χ^2 statistic:

$$\chi^2(\mathbf{p}_{\text{mean}} | M_1, M_2, z) = \sum_i \frac{[\langle v_{r,\text{sim}} \rangle(r_i) - \langle v_{r,\text{mod}} \rangle(r_i | \mathbf{p}_{\text{mean}})]^2}{\sigma_{r,\text{sim}}^2(r_i) / N_{\text{pairs}}(r_i)}, \quad (34)$$

where $\langle v_{r,\text{sim}} \rangle(r_i)$ is the mean radial velocity profile at the i -th radius in the simulation, $\langle v_{r,\text{mod}} \rangle(r_i)$ is the counterpart of our model prediction, $\mathbf{p}_{\text{mean}} = (\mathcal{A}_\rho, \mathcal{B}_\rho, \mathcal{C}_\rho)$, $\sigma_{r,\text{sim}}(r_i)$ is the dispersion of v_r at the i -th radius, and $N_{\text{pair}}(r_i)$ is the number of pairs in the i -th radius. Once the best-fit \mathbf{p}_{mean} is found, we then minimize other χ^2 quantities to find the best-fit parameters in Eq. (24):

$$\chi^2(\mathbf{p}_\alpha | M_1, M_2, z) = \sum_i \frac{[\sigma_{\alpha,\text{sim}}^2(r_i) - \sigma_{\alpha,\text{mod}}^2(r_i | \mathbf{p}_\alpha)]^2}{2\sigma_{\alpha,\text{sim}}^4(r_i) / N_{\text{pairs}}(r_i)}, \quad (35)$$

where $\alpha = t$ or r , $\sigma_{\alpha,\text{sim}}^2(r_i)$ is the velocity dispersion profile at the i -th bin radius, $\sigma_{\alpha,\text{mod}}^2(r_i)$ is the our model prediction, $\mathbf{p}_t = (\mathcal{C}_t^{(0)}, \mathcal{C}_t^{(1)}, p_t)$ and $\mathbf{p}_r = (\mathcal{C}_r^{(0)}, \mathcal{C}_r^{(1)}, \mathcal{C}_r^{(2)})$.

In the calibration process, we find that the minimum χ^2 per the number of degree of freedoms ranges from 1 to 10^4 , while it depends on halo masses and redshifts. Note that our fitting assumes zero covariances among different radii and Gaussian errors for velocity moments. Because we work on non-linear scales of $\mathcal{O}(10) h^{-1} \text{Mpc}$, these assumptions are expected to be invalid to have an appropriate χ^2 . The goodness-of-fit based on χ^2 will be meaningful when the error bars are precisely estimated. Hence, the minimum χ^2 value in our fitting should be taken as just a reference.

Given the sets of \mathbf{p}_{mean} , \mathbf{p}_t , \mathbf{p}_r as a function of M_1 , M_2 , and z , we then find an appropriate form to smoothly interpolate the data points after trial and error. For an example, we assume that the form of $B_\rho(M_1, M_2, z)$ is given by $B_0(z) [(M_1 + M_2) / 10^{13} h^{-1} M_\odot]^{B_1(z)}$. We then find the best-fit B_0 and B_1 for a given z by a least-square fitting with

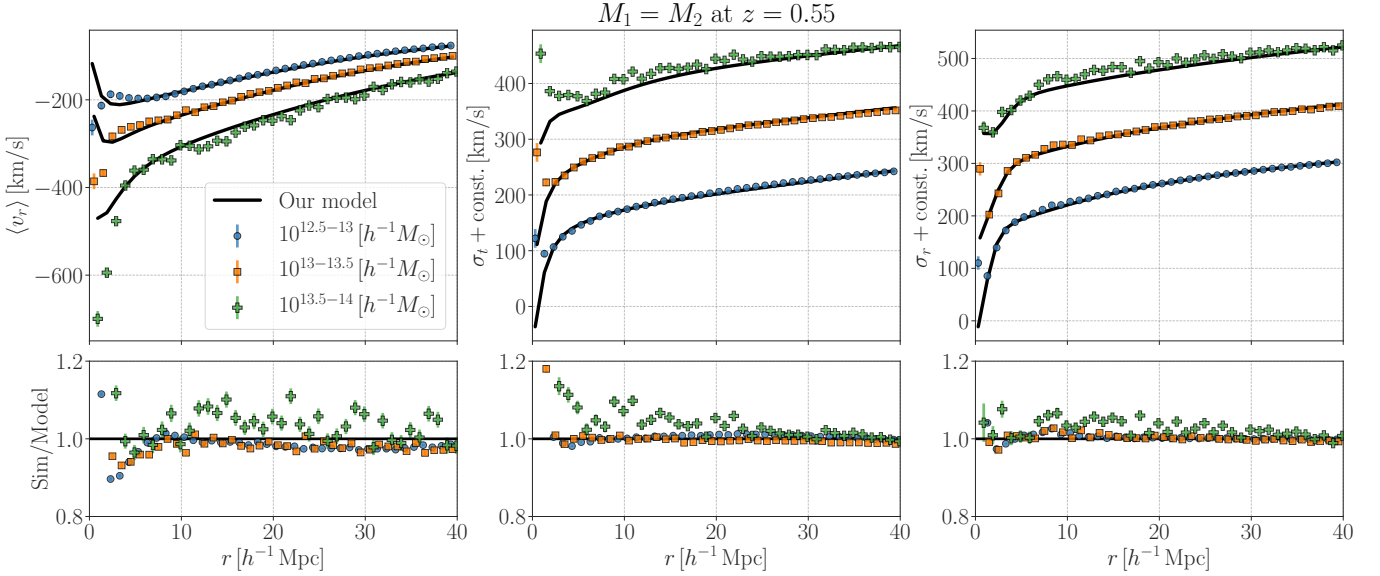


Figure 2. The mean and dispersions of pairwise velocities of dark matter halos at $z = 0.55$. We here focus on the halo samples with $M = M_1 = M_2 = 10^{12.5-13}, 10^{13-13.5}$, and $10^{13.5-14} h^{-1} M_\odot$. In each panel, the blue circle, orange square, and green plus symbols represent the simulation results for $M = 10^{12.5-13}, 10^{13-13.5}$, and $10^{13.5-14} h^{-1} M_\odot$, respectively. The model predictions are shown in the solid lines. The error bar in each panel shows the Gaussian error at a given radius. The upper three panels present the profiles of mean radial velocity, the dispersions of the tangential and radial components, while the lower panels show the ratio between the simulation results and our model prediction. Note that the Gaussian error in each panel is too small to plot for most cases. For visualization purpose, we shift the profiles of $\sigma_{t,r}$ by -100 and $+100$ km/s for the sample of $M = 10^{12.5-13}$ and $10^{13.5-14} h^{-1} M_\odot$, respectively.

the measured $B_\rho(M_1, M_2, z)$. The redshift dependence of B_0 and B_1 is then derived by a quadratic function fit. The details of our functional forms for other parameters are provided in Appendix A⁸. It is obvious that our calibration process can be affected by details of the interpolation of \mathbf{p}_{mean} , \mathbf{p}_t , and \mathbf{p}_r (e.g. a choice of the functional form). This point is discussed in Section 6.3.

5. RESULTS

Here we present the comparison of the pairwise velocity statistics from our model with the simulation results. We pay a special attention to the results at $z = 0.55$, because it is relevant to the CMASS sample in the SDSS-III BOSS. We then discuss the information content in redshift-space clustering in terms of the pairwise velocity statistics.

5.1. Velocity moments for galaxy- and group-sized halos

We first show the results of the first three non-zero moments of the pairwise velocity for the halo samples with their masses of $10^{12.5-13}, 10^{13-13.5}$, and $10^{13.5-14} h^{-1} M_\odot$. Figure 2 summarizes the comparisons of $\langle v_r \rangle$, σ_t , and σ_r from our model with the simulation results. In the range of $5 \lesssim r [h^{-1} \text{Mpc}] < 40$, our model can reproduce the mean and dispersion of the pairwise velocity of the simulated halos with $10^{12.5} < M [h^{-1} M_\odot] < 10^{13.5}$ within a 5%-level precision, while still providing a reasonable fit to the results for group-sized halos with $10^{13.5} < M [h^{-1} M_\odot] < 10^{14}$. According to the Gaussian error estimate, our measurement of velocity moments in simulations is precise with a level of $< 5\%$ for $M < 10^{14} h^{-1} M_\odot$ and $z < 1$. The number of halo pairs including halos of $M > 10^{14} h^{-1} M_\odot$ at $z = 1.01$ becomes small, but our measurements reach a 15%-level precision even at halo pairs with their masses of $< 10^{14.5} h^{-1} M_\odot$ at $z = 1.01$.

The comparisons in Figure 2 demonstrate that our model in Section 2 is efficient and flexible enough at $z = 0.55$ and a selection of mass bins to explain the radial profiles of the mean and dispersion of the pairwise velocity in the

⁸ We also make our pipeline for the calibration process publicly available at https://github.com/shirasakim/Fitting_velocity_moments_T07.

simulated halos for all but the small scales of $r < 5 [h^{-1} \text{Mpc}]$. For other redshifts and halo masses, we summarize the comparisons in Appendix C. We confirm that our model can reproduce the velocity-moment profiles with a 5%-level precision for $10^{12.5} < M [h^{-1} M_{\odot}] < 10^{13.5}$ at $0.3 < z < 1$, and the model precision reaches a 20% level at the very worst in other ranges of halo masses and redshift.

5.2. Mass-limited samples

We then move onto the comparisons of various velocity statistics for the mass-limited halo samples. Because our calibration process includes the interpolation of model parameters as a function of halo mass and redshift, it is important to check if our model still works for samples with a wider range of halo masses.

5.2.1. Pairwise-velocity distribution and its moments

Figure 3 shows the comparisons of the velocity PDFs in the simulation with our model prediction. In each panel, the gray and black solid lines represent the model predictions for v_r and v_t , respectively. For a comparison, we show the predictions by the model in Tinker (2007) by the gray and black dashed lines. Although our model has been calibrated by the measurements of the three velocity moments as in Eqs. (31)-(33), the non-Gaussian tails in the PDFs can be explained by our model in a reasonable way. This indicates that a large part of the non-Gaussianity in the velocity PDFs can be related with the non-Gaussianity in the cosmic mass density (see Tinker 2007, for further discussion).

Compared to the previous work, our model can provide a better fit to the velocity dispersion of v_t as well as the long tails in PDFs for a wide range of r . We find that the mean and velocity dispersion can be explained by our model within a 10% level for the mass-limited sample with $M \geq 10^{13.5} h^{-1} M_{\odot}$. This is clearly shown in Figure 4 and valid for the redshifts of $z = 0.3$ and 1.01. For the mass-limited sample with $M \geq 10^{12.5} h^{-1} M_{\odot}$, we find that our model is in good agreement with the simulation results and the precision reaches a 5% level in the range of $5 < r [h^{-1} \text{Mpc}] < 40$.

5.2.2. Two-point clustering analyses in redshift space

We next examine a more practical analysis of the two-point correlation function in redshift space, denoted by $\xi_{\text{gg}}^S(s_p, s_{\pi})$, for the mass-limited samples. Note that we suppose the real-space correlation function is known in this paper, while we study the mapping of the correlation function between real and redshift space by our model of the velocity PDFs (see Eq. [3]). The details about modeling of the velocity PDF with a HOD are summarized in Appendix B.

Figure 5 shows the comparisons of ξ_{gg}^S between the simulation results and the model predictions. For the model prediction of ξ_{gg}^S , we use the real-space correlation function measured in the simulations and interpolate the data points over separation lengths r . We find that our model can provide a more reasonable fit to ξ_{gg}^S in the simulations than the models by Tinker (2007). In particular, our model improves the mapping at small s_{π} , because our model shows a better fit to the velocity dispersion of v_t in the simulations and v_t is relevant to the line-of-sight velocity at small s_{π} .

For a more quantitative view, we show comparisons of the clustering multipoles defined in Eq. (29). Figure 6 summarizes comparisons for the mass-limited sample with $M \geq 10^{13.5} h^{-1} M_{\odot}$. The figure clearly shows that our model can provide an accurate mapping of the two-point correlation function between real and redshift space at intermediate scales of $\sim 10 h^{-1} \text{Mpc}$. For the lowest-order moment, our model can provide an excellent fit to the simulation results within a 5% level over $5 < s [h^{-1} \text{Mpc}] < 40$. Even for the higher-order moments, we find that our model can explain $\xi_2(s)$ and $\xi_4(s)$ in the range of $10 - 30 h^{-1} \text{Mpc}$ with a 10%- and 50%-level precision, respectively. For the mass-limited sample with $M \geq 10^{12.5} h^{-1} M_{\odot}$, the agreement is found to be worse compared to the samples with $M \geq 10^{13.5} h^{-1} M_{\odot}$. Nevertheless, the lowest moment ξ_0 can still be reproduced by our model within a 5% level precision over $3 < s [h^{-1} \text{Mpc}] < 30$ even for the sample with $M \geq 10^{12.5} h^{-1} M_{\odot}$.

5.3. Realistic galaxy samples

Here we present the results for a realistic galaxy mock sample with the HOD model in Section 3.2. Figure 7 summarizes the comparisons of the velocity-moment profiles in the simulation with our model predictions. We find that our model can provide a few-percent-level prediction of the mean radial velocity as well as the velocity dispersions for CMASS-like galaxies at $5 - 40 h^{-1} \text{Mpc}$.

For the clustering multipoles, figure 8 shows the comparisons between the simulation results and our model predictions. The red solid lines in the figure represent our model predictions, while the dashed line shows the so-called two-halo terms in a halo-model approach (see Appendix B for details). In our halo model, the redshift-space clustering

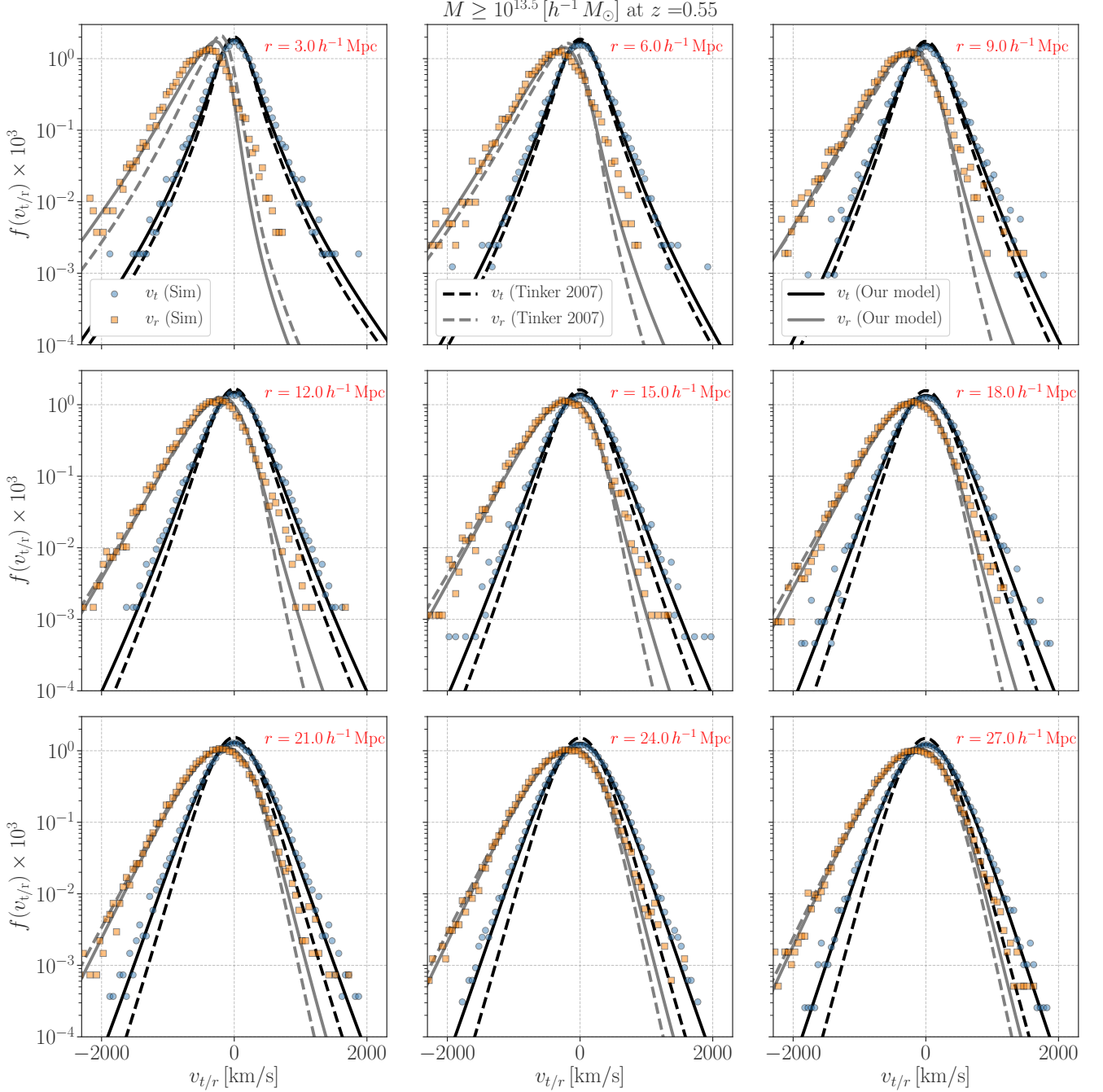


Figure 3. The probability distribution functions (PDFs) of the pairwise velocity of dark matter halos with their masses greater than $10^{13.5} h^{-1} M_{\odot}$ at the redshift of 0.55. The nine panels show the PDFs at different separation length, r (labeled at the top right in each panel). In each panel, the blue circle and orange square symbols show the PDFs of v_t and v_r in the simulation, respectively. Our model predictions are shown in the black and gray solid lines in each panel, while the dashed lines represent the models in Tinker (2007). Our model improves the precision for the velocity dispersion of v_t as well as the mean velocity of v_r compared to the model in Tinker (2007). Note that we do not introduce any parameters to explain the skewness and kurtosis in our model, and any non-Gaussian features in the PDFs come from non-Gaussianity in the cosmic mass density (see Section 2 for our model).

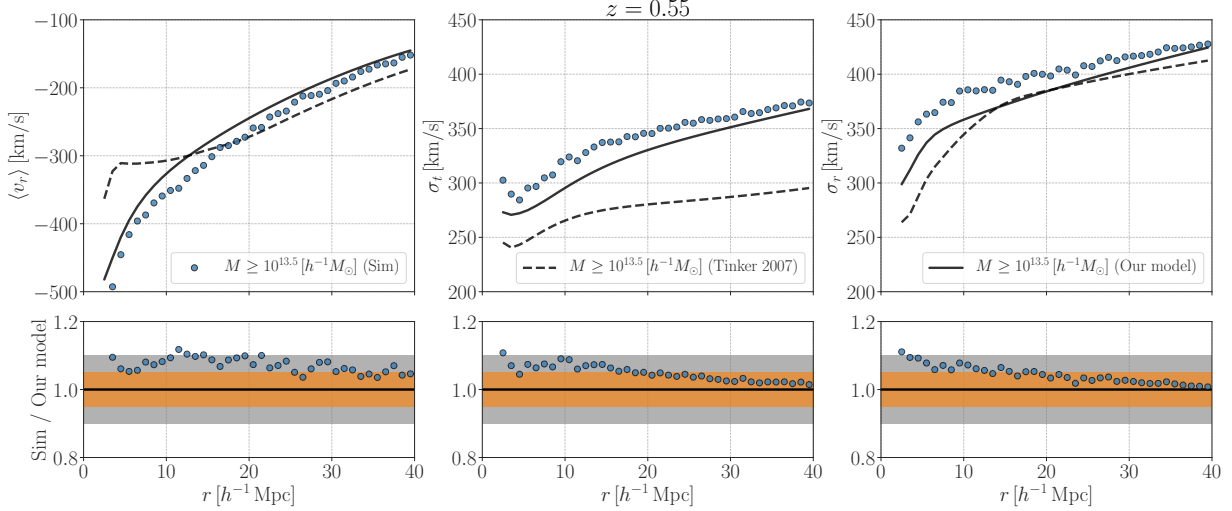


Figure 4. Similar to Figure 2, but for a mass-limited sample of halos. Here we plot the mean and dispersion of pairwise velocity of dark matter halos with their masses greater than $10^{13.5} h^{-1} M_{\odot}$ at the redshift of 0.55. In the upper three panels, the blue circles show the simulation results, while the solid and dashed lines represent the predictions by our model and Tinker (2007), respectively. In the lower panels, we show the ratio between the simulation result and our model. For a reference, the gray regions show $\pm 10\%$ levels, while the yellow one stands for $\pm 5\%$ levels.

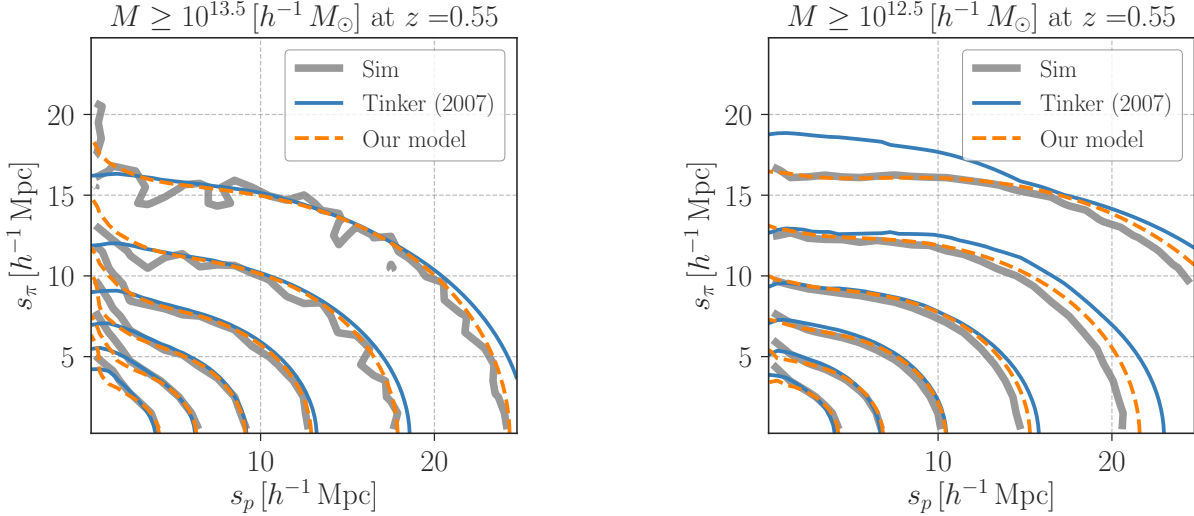


Figure 5. Two-dimensional redshift-space correlation functions of mass-limited halo samples at $z = 0.55$. The left panel shows the result for $M \geq 10^{13.5} h^{-1} M_{\odot}$, while the right stands for $M \geq 10^{12.5} h^{-1} M_{\odot}$. In each panel, the gray lines show the contours of the redshift-space correlation of $\xi_{\text{gg}}^S(s_p, s_{\pi})$, and the orange dashed lines are the model predictions by our model. For a comparison, the blue solid lines shows the model by Tinker (2007). In each panel, the contours are separated by factors of 1.9 for clarity. The outermost represents $\xi_{\text{gg}}^S(s_p, s_{\pi}) = 1.9^{-1.5}$ and $1.9^{-3.5}$ in the left and right panels, respectively.

multipoles can be decomposed into two parts:

$$\xi_{\ell}(s) = \xi_{\ell,1\text{h}}(s) + \xi_{\ell,2\text{h}}(s) \quad (36)$$

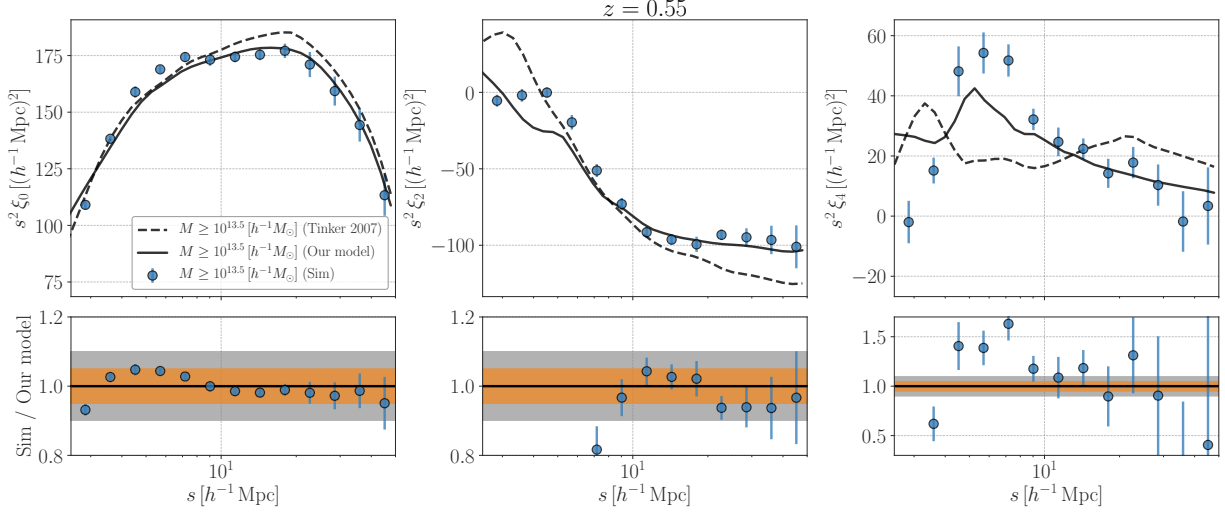


Figure 6. Redshift-space clustering multipoles of the mass-limited halo sample with $M \geq 10^{13.5} h^{-1} M_{\odot}$ at $z = 0.55$. The upper panels show the multipole moments of ξ_0 , ξ_2 and ξ_4 from left to right. In each upper panel, the blue points with error bars show the simulation results, while the solid and dashed lines represent the predictions by our model and Tinker (2007), respectively. In the lower panels, we show the ratio of the simulation results and our model predictions. The yellow and gray filled regions show $\pm 5\%$ - and $\pm 10\%$ -level differences.

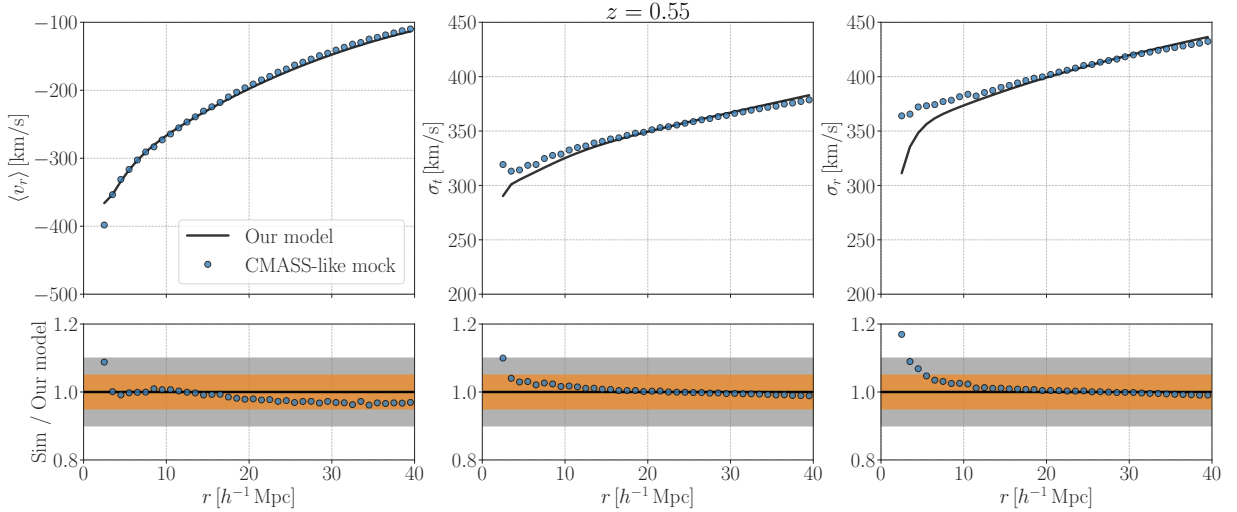


Figure 7. Similar to Figure 4, but for a mock sample of CMASS galaxies at $z = 0.55$. In each panel, the blue points show the simulation results, while the solid lines represent our model predictions. Note that the typical halo mass of CMASS galaxies is set to $\sim 10^{13} h^{-1} M_{\odot}$, but we include the satellite galaxies for $M > 10^{13.27} h^{-1} M_{\odot}$.

where $\xi_{\ell,1h}$ represents the two-point correlation in single dark matter halos, $\xi_{\ell,2h}$ is the contribution from the clustering between two neighboring halos. The one-halo term $\xi_{\ell,1h}$ can be further divided into two contributions from the central-satellite and satellite-satellite pairs. The two-halo term $\xi_{\ell,2h}$ is mostly determined by the clustering and streaming motion of the central-central pairs, but it is also affected by the velocity dispersion of satellites in single halos. Our model predictions are in good agreement with the simulation results at the scales of $s \gtrsim 10 h^{-1} \text{Mpc}$, i.e. the regime where the two-halo contributions would play a central role. Note that the inaccurate small-scale two-halo term can

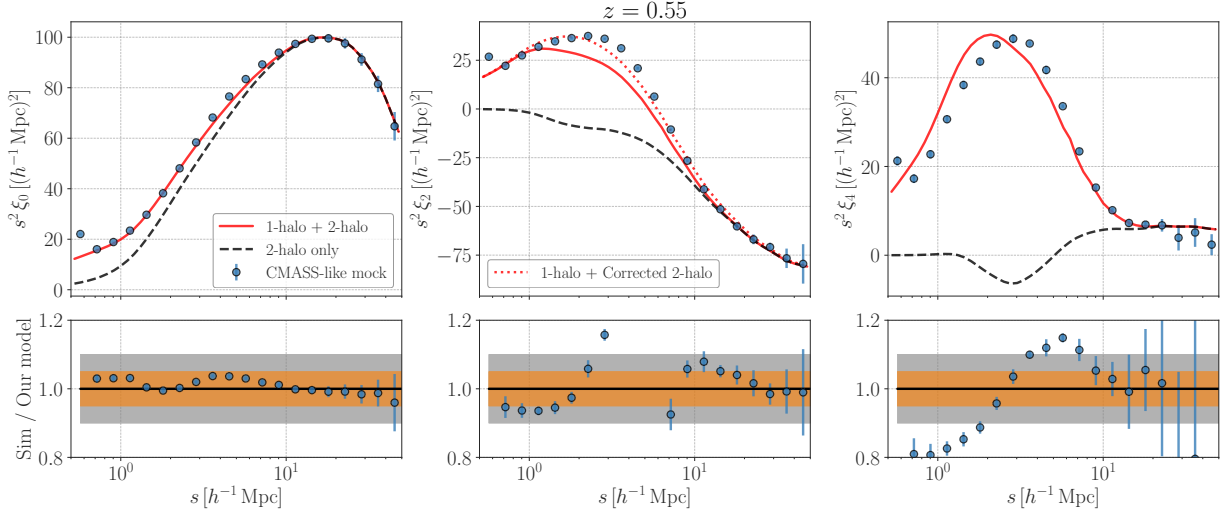


Figure 8. Similar to Figure 6, but for a mock sample of CMSS galaxies at $z = 0.55$. In each panel, the blue points with error bars are the simulation results, while the red solid line shows the model predictions based on the HOD and our model of the pairwise velocity PDFs. For a comparison, the dashed lines show the two-halo contribution to the multipole moments. In the top middle panel, the red dotted line shows the model with the correction as in Eq. (37).

affect the prediction of $\xi_2(s)$ at $s \sim 3 - 5 h^{-1}\text{Mpc}$. We find that a simple modification in the two halo term of ξ_2 can provide a better fit to the simulation:

$$\xi_{2,2h}(s) \rightarrow \exp \left[- \left(\frac{s_{\text{cut}}}{s} \right)^2 \right] \xi_{2,2h}(s), \quad (37)$$

where s_{cut} is a free parameter and we find $s_{\text{cut}} \sim 3.5 h^{-1}\text{Mpc}$ is appropriate for our mock catalog. The two-halo term $\xi_{2,2h}$ at $s < 10 h^{-1}\text{Mpc}$ would be affected by the non-Gaussianity in the pairwise velocity PDFs (e.g. Cuesta-Lazaro et al. 2020). Our model has been calibrated to explain the mean and variance in the pairwise velocity PDF at $5 < r [h^{-1}\text{Mpc}] < 40$. After the calibration, we found that it fails to provide a fit to the PDF at $r < 5 h^{-1}\text{Mpc}$ (e.g. see the top left panel in Figure 3). Hence, we expect that our model can not work for the precise prediction of $\xi_{2,2h}$ at $s < 10 h^{-1}\text{Mpc}$. Nevertheless, including a single nuisance parameter s_{cut} can improve our model precision for ξ_2 at $s = 1 - 10 h^{-1}\text{Mpc}$.

5.4. Information contents of redshift-space clustering multipoles

For an application of our model, we discuss the information content in redshift-space clustering analyses of galaxies. According to Eq. (3), the observed two-point correlation function in redshift space should contain the information about the pairwise velocity statistics of galaxies. At intermediate scales of $\sim 10 \text{Mpc}$, a class of modified gravity theory predicts that the mean and dispersion of the pairwise velocity for massive-galaxy-sized halos can differ from the prediction from General Relativity by 10 – 20% (e.g. Hellwing et al. 2014; Zu et al. 2014). For the galaxy-halo connection, numerical simulations have shown that the pairwise velocity statistics for realistic galaxies can depend not only on their host halo masses but also the inner mass density profiles of their host halos and ages (e.g. Hearin 2015; Padilla et al. 2019). This is known as the assembly bias effect.

As a simple example, we study the modified gravity effect and/or the assembly bias effect on the halo pairwise velocity by introducing two free parameters:

$$v_z^{\text{obs}} = b_{v0} \langle v_z \rangle + b_{v1} (v_z - \langle v_z \rangle), \quad (38)$$

where v_z^{obs} represents the line-of-sight pairwise velocity affected by the modified gravity and/or the assembly bias effect, while v_z is a baseline prediction in the ΛCDM cosmology. We here assume that statistical properties of v_z can be characterized by halo masses, redshifts, and separation lengths. Note that b_{v0} changes the mean pairwise velocity

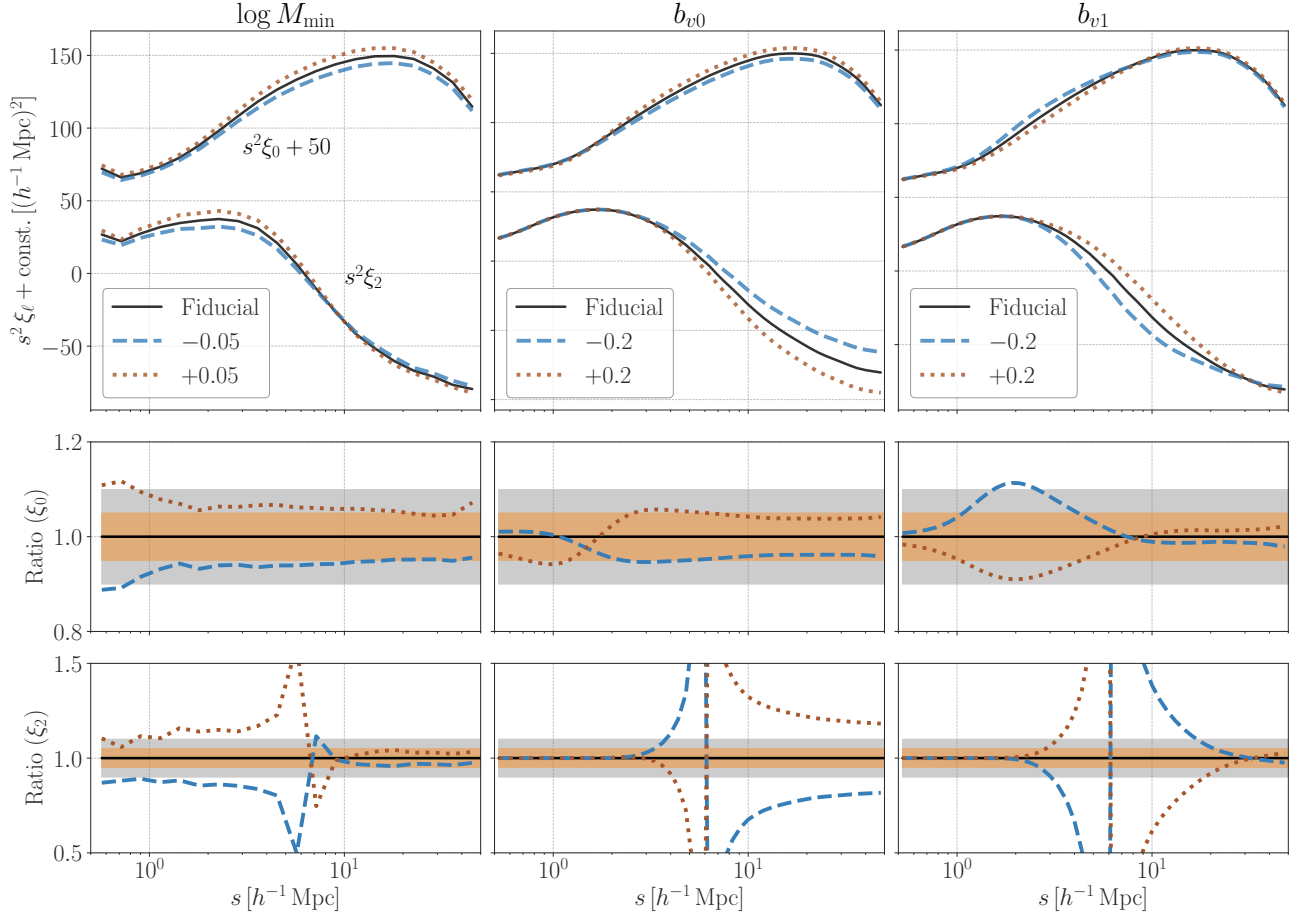


Figure 9. Dependence of redshift-space clustering multipoles on a HOD parameter and velocity biases. In the three top panel, we show the monopole ξ_0 and quadrupole ξ_2 for the CMASS-like mock galaxies at $z = 0.55$ when varying the HOD parameter $\log M_{\min}$ and the velocity-bias parameters b_{v0} and b_{v1} from left to right. The definitions of b_{v0} and b_{v1} are found in Section 5.4. In each panel, the black solid lines show the results for our fiducial set of the parameters, while the blue dashed and red dotted lines represent the responses of $\xi_{0,2}$ when we vary the parameters. In the three middle panels, we summarize the ratio of $\xi_{0,2}$ with respect to the fiducial results. We also show the ratio of ξ_2 in the three bottom panels. For references, the gray and yellow filled regions in the middle and bottom panels show $\pm 10\%$ - and $\pm 5\%$ -level differences, respectively.

for a given galaxy sample, while b_{v1} affects the variance in the pairwise velocity. The modified gravity and/or the assembly bias can deviate b_{v0} and b_{v1} from unity. Therefore, it would be interesting to consider the dependence of the clustering multipoles of $\xi_{0,2}$ on the velocity-bias parameters b_{v0} and b_{v1} . We here emphasize that our velocity biases in Eq. (38) have a different meaning from the common definitions in the literature. Previous studies have mainly focused on the velocity biases with respect to the core or the kinematics of dark matter inside the single dark matter halo (e.g. Reid et al. 2014; Guo et al. 2015). In contrast, our parameterization of the velocity bias enables us to study the bias in the streaming motion between two neighboring halos⁹. Using Eq. (38) and the formulas in Appendix B, we compute the expected signal of $\xi_{0,2}$ for the HOD model in Section 3.2 as a function of b_{v0} and b_{v1} . To check for degeneracy among the HOD parameters, we also vary a parameter of $\log M_{\min}$ which determines the typical halo mass of galaxy sample of interest. We generated two additional mock galaxy catalogs using the ν^2 GC-L simulation by changing the parameter of $\log M_{\min}$ by ± 0.05 . In the following, we use these simulation results when studying the effect of $\log M_{\min}$.

⁹ Within our framework, non-trivial galaxy-halo connection may induce biases in the streaming motion between two galaxies. An example is the environmental dependence of HODs (e.g. Hadzhiyska et al. 2020). If the HOD depends not only on the halo mass but also the environmental density δ , the pairwise velocity statistics can differ from our predictions. We also expect that a modification of gravity can change the relation of the mean infall velocity and density perturbations (see, e.g. Li & Efstathiou 2012, for the spherical collapse model in a modified gravity theory), leading to $b_{v0} \neq 1$.

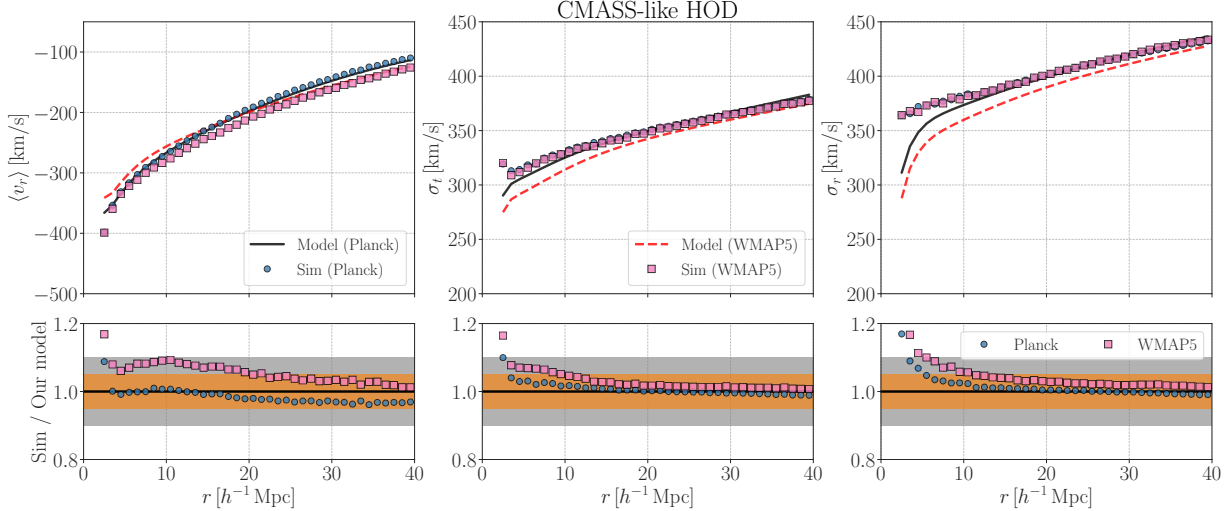


Figure 10. Similar to Figure 7, but we include the comparison with the results from the MultiDark simulation at $z = 0.534$ and our model predictions. In this figure, we consider the mock galaxy sample with the HOD model in Section 3.2. Note that our fiducial simulation assumes the cosmological model inferred by the Planck satellite ($\Omega_{m0} = 0.31$ and $\sigma_8 = 0.83$), while the MultiDark run assumes the model with $\Omega_{m0} = 0.27$ and $\sigma_8 = 0.82$. In the upper panels, the blue circle and pink square symbols represent the simulation results in the Planck and WMAP5 cosmology, respectively. The solid line shows our model prediction for the Planck cosmology, while the red dashed line is the model prediction for the WMAP5 cosmology.

When varying the biases of b_{v0} and b_{v1} , we use the analytic model of the pairwise velocity PDF as in Appendix B and predict the multipoles based on Eq. (3). We also adopt the correction in Eq. (37) for our model of the two-halo term in ξ_2 .

Figure 9 summarizes the changes in $\xi_{0,2}$ for the CMASS-like galaxy sample at $z = 0.55$ caused by differences in $\log M_{\min}$, b_{v0} and b_{v1} . In the figure, we set the HOD parameters as in Section 3.2 and $b_{v0} = b_{v1} = 1$ for the fiducial case. The figure indicates that the effect of b_{v0} and b_{v1} on the redshift-space clustering can not be compensated for by simple changes in the typical host halo mass. When it comes to other HOD parameters, we find that $\sigma_{\log M}$ and M_1 show a strong degeneracy with $\log M_{\min}$, while M_{cut} and α_M can change the one-halo term while changing two-halo term minimally. We also note that the real-space correlation function strongly depends on the HOD parameters, but is independent of the biases of b_{v0} and b_{v1} . The real-space correlation function can be reproduced within the HOD framework for a given cosmological model and the HOD parameters have been tightly constrained with the combined analysis of galaxy-galaxy lensing and projected correlation functions (e.g. More et al. 2015). Therefore, we expect that a joint analysis of $\xi_{0,2}$ with galaxy-galaxy lensing and projected correlation functions provides an important test of the common HOD framework with no assembly biases at least. For more details (e.g. expected constraints of b_{v0} and b_{v1} for a given galaxy sample), we require a precise estimate of the covariance of $\xi_{0,2}$ and leave it for future studies.

6. LIMITATIONS

We summarize the major limitations in our model of pairwise velocity PDFs of dark matter halos. All of the following issues will be addressed in forthcoming studies.

6.1. Cosmological dependence

Our model of pairwise velocity PDFs is calibrated against N -body simulations in the Λ CDM cosmology consistent with Planck. In terms of studies of large-scale structure, Ω_{m0} and σ_8 are the primary parameters and the simulations in this paper adopt $\Omega_{m0} = 0.31$ and $\sigma_8 = 0.83$. Therefore, our functions in Section 2 and Appendix A may be subject to an overfitting to the specific cosmological model. To examine the dependence of our model on cosmological models, we use another halo catalog from N -body simulations with a different Λ CDM model. For this purpose, we use the first MultiDark simulation performed in Prada et al. (2012). The MultiDark simulation consists of 2048^3 particles in a volume of $1 [h^{-1}\text{Gpc}]^3$ and assumes the cosmological parameters of $\Omega_{m0} = 0.27$, $\Omega_{b0} = 0.0469$, $\Omega_{\Lambda} = 1 - \Omega_{m0} = 0.73$,

$h = 0.70$, $n_s = 0.95$, and $\sigma_8 = 0.82$. These are consistent with the five-year observation of the cosmic microwave background obtained by the WMAP satellite (Komatsu et al. 2009) and we refer to them as the WMAP5 cosmology. We use the ROCKSTAR halo catalog at $z = 0.534$ from the MultiDark simulation¹⁰ and then produce a CMASS-like mock catalog by using the HOD model in Section 3.2. To compute our model prediction for the WMAP5 cosmology, we fix the functional forms and parameters in Appendix A but include the cosmology-dependence of the log-normal PDF of cosmic mass density, the linear halo bias and the linear growth factor, accordingly. In other words, we assume the model in Appendix A is universal and valid for different cosmological models.

Figure 10 summarizes the velocity-moment profiles of the CMASS-like mock catalog for two different cosmologies. In this figure, the solid and red dashed lines show the predictions by our model for the Planck and WMAP5 cosmologies, respectively. We find that our model can reproduce simulation results within a 5-10% level even for the WMAP5 cosmology at $5 - 40 h^{-1}\text{Mpc}$. It is worth noting that the cosmological dependence of the velocity dispersion is small in the simulations, but our model predicts a few percent level difference. For the mean radial velocity profile, we find a 10%-level difference between the simulation and our model in the WMAP5 cosmology at $r < 20 h^{-1}\text{Mpc}$, while our model provides a better fit to the simulations at larger scales of $r \gtrsim 25 h^{-1}\text{Mpc}$. For comparison, our model can predict the mean radial velocity profile at $r = 5 - 40 h^{-1}\text{Mpc}$ within a 5%-level precision in the Planck cosmology.

In summary, our model can not predict the simulation results for the WMAP5 cosmology with the same level as in the Planck cosmology. The 10%-level difference in Ω_{m0} can cause systematic uncertainties in our model predictions with a level of 5-10%. Note that the velocity dispersions are found to be less sensitive to the change in Ω_{m0} in the simulations. More extensive studies are required to investigate the cosmological dependence of the pairwise velocity statistics.

6.2. Calibrations with N -body particle data

Our model assumes that the pairwise velocity PDFs can be expressed as a Gaussian at a given environmental density δ . Tinker (2007) already showed that the approximation looks valid by using the N -body simulations, while the δ dependence of the Gaussian parameters (mean and variance) may be different from our assumptions in Eqs. (18) and (23). We also assume that the conditional PDF of cosmic mass density finding a halo pair is given by the form of Eq. (8), but another functional form would provide a better fit to the simulation results at small scales. The calibration with the information of N -body particles is important to validate the underlying assumptions in our model.

After the calibration, we find that our model can not provide a reasonable fit to the pairwise velocity PDF of mass-limited halos at $z = 0$. Figure 11 summarizes the pairwise velocity PDFs for the mass-limited sample with $M \geq 10^{13.5} h^{-1}M_\odot$ at $z = 0$. The figure shows sizable differences of radial velocity PDFs between our model and the simulation results. Note that the standard deviation $\sigma_{r,t}$ can be explained by our model within a 5%-level precision for this mass-limited sample, but the mean radial velocity profiles in the simulation are larger than our model predictions by $\simeq 30\%$. Because the mean velocity profile in our model is sensitive to the functional forms in Eqs. (8) and (23), the additional information of N -body particles allows us to find more appropriate functional forms. Also, our model can not explain the velocity-moment profiles at $r \lesssim 5 h^{-1}\text{Mpc}$ for most cases. This also implies that Eqs. (18) and (23) may need some corrections for the velocity statistics at $r \lesssim 5 h^{-1}\text{Mpc}$. Note that the log-normal approximation for the cosmic mass density PDF can be less accurate at the scale of $r \lesssim 5 h^{-1}\text{Mpc}$ (e.g. Shin et al. 2017).

6.3. Interpolation errors and more precise modeling

As in Section 4, our calibration is based on the least square fitting of velocity-moment profiles and the interpolation of the best-fit parameters over halo masses and redshifts. Our interpolation scheme provides the best performance for dark matter halos with $10^{12.5} < M [h^{-1}M_\odot] < 10^{13.5}$ at $0.3 < z < 1$, but it gives less precise predictions for other ranges of M and z . Figure 12 summarizes an example of the interpolation error in our calibration process. In this figure, we show the velocity-moment profiles for halos with $M = 10^{13.5-14} h^{-1}M_\odot$. After the fitting process, we find the best-fit expression of each profile as shown in the orange lines of Figure 12. Since the final model involves with interpolation of model parameters over M and z , sizable residuals can be found in the comparisons of velocity-moment profiles if we use an inaccurate interpolation method. Figure 12 also highlights that the best-fit expression reaches a few-percent-level precision for a given bin of masses and redshift. This indicates that a more sophisticated interpolation beyond the use of an analytic function will further improve the precision of our model prediction.

¹⁰ The halo catalogs at different redshifts are publicly available at https://slac.stanford.edu/~behroozi/MultiDark_Hlists_Rockstar/.

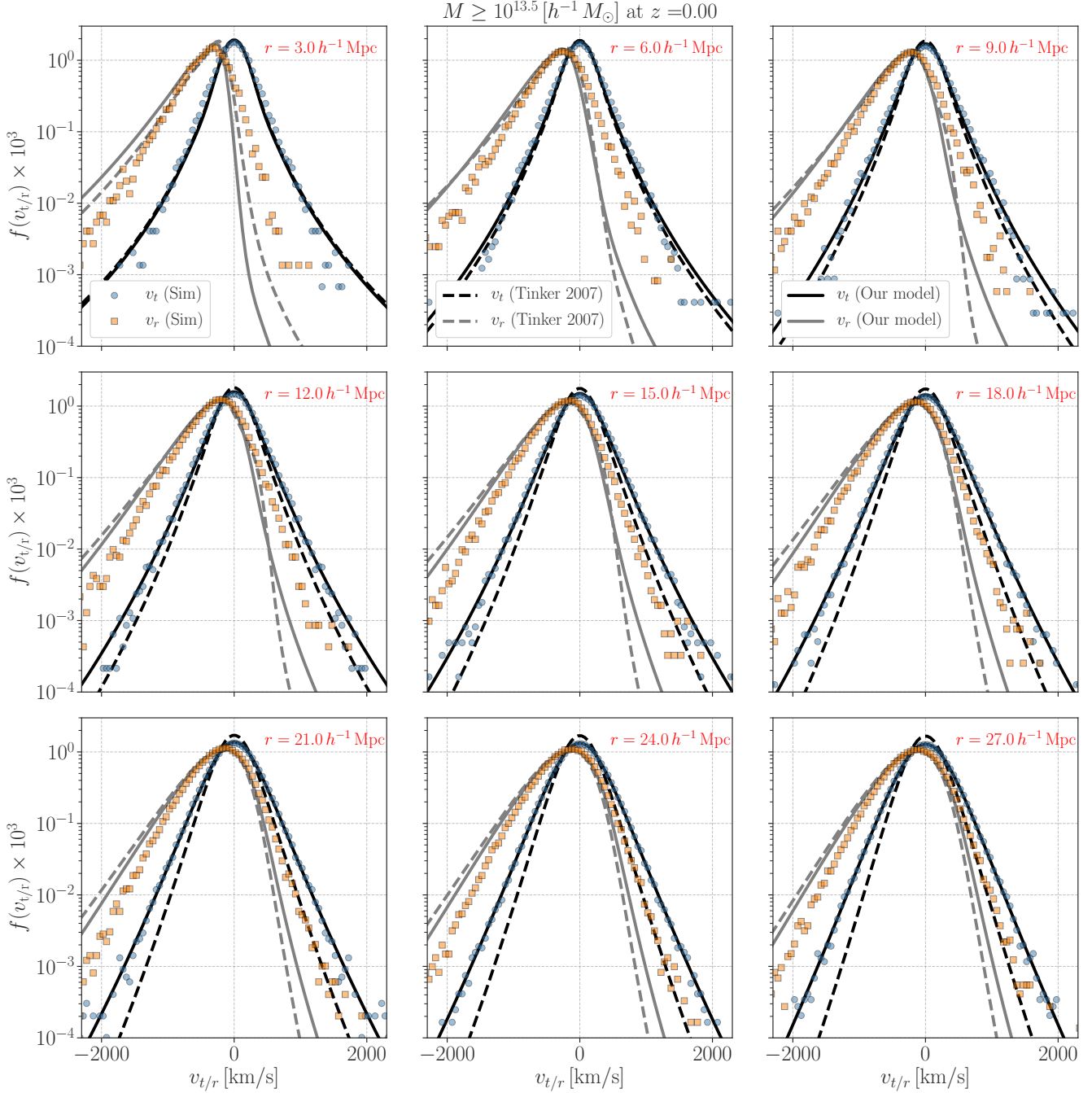


Figure 11. Similar to Figure 3, but we here show the probability distribution functions (PDFs) of the pairwise velocity of dark matter halos with their masses greater than $10^{13.5} h^{-1} M_{\odot}$ at the redshift of 0.

A promising approach for the interpolation of our model parameters is the Gaussian Process Regression. The Gaussian Process Regression allows to interpolate a large-dimensional dataset in a non-parametric way and it is becoming a standard approach to develop accurate models for various statistics of large-scale structures (e.g. [Habib et al. 2007](#); [Lawrence et al. 2010](#); [Kwan et al. 2013, 2015](#); [McClintock et al. 2019](#); [Nishimichi et al. 2019](#)). For the Gaussian Process Regression, one usually needs to reduce the effective numbers of data points in some way such as the Principle Component Analysis. In our approach, we can reduce the number of model parameters in a physically-

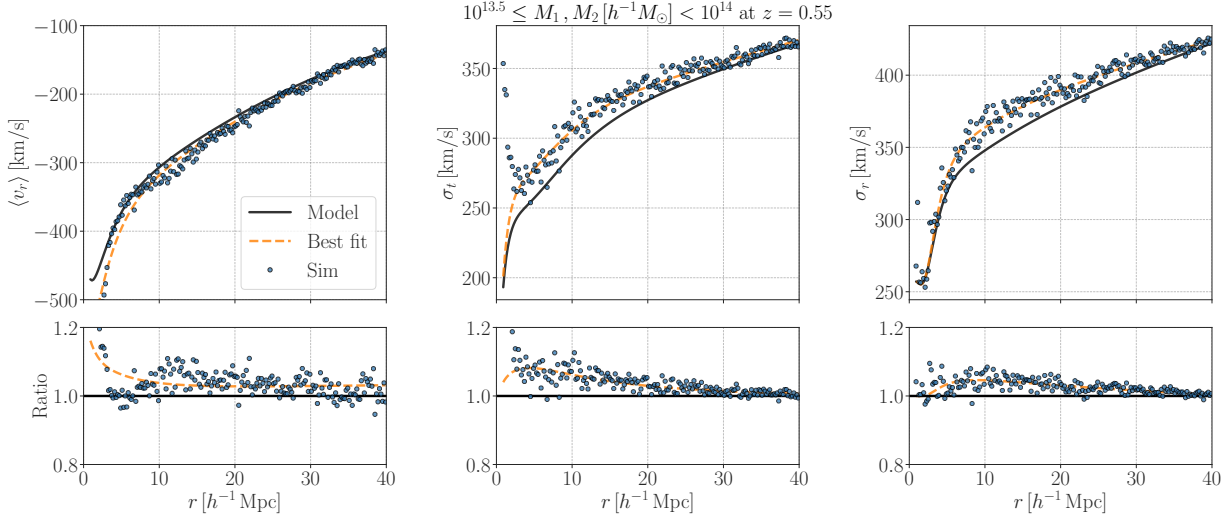


Figure 12. Interpolation error in our model of the pairwise velocity PDFs. In the upper panels, the blue points show the velocity-moment profiles of $\langle v_r \rangle$, σ_t , and σ_r for the halos with $M_1 = M_2 = 10^{13.5-14} h^{-1} M_\odot$ at $z = 0.55$, while the solid lines are our model predictions. The orange line shows the best-fit model inferred by the least-square fitting of velocity moment profiles in the calibration process (see Section 4 for details). In the bottom, we show the ratio of profiles between simulation results and our model with the blue points, while the orange line shows the ratio between the best-fit and our model which includes the interpolation over halo masses.

motivated way. Our analyses show that only three functions, $\tilde{\rho}_0(r, M_1, M_2, z)$, $\tilde{\rho}_t(r, M_1, M_2, z)$ and $\tilde{\rho}_r(r, M_1, M_2, z)$ (see Section 2 for details) will be sufficient to fit the pairwise velocity PDFs for the Planck cosmology.

It would be worth mentioning that this is a huge reduction of the number of dimensions in the model compared to other models of pairwise velocity PDFs in the literature. [Zu & Weinberg \(2013\)](#) introduced a two-dimensional skewed-t distribution with seven functions to explain the pairwise velocity PDFs of galaxies around clusters. The seven functions in [Zu & Weinberg \(2013\)](#) depend on r, M_1, M_2 and z in principle. [Bianchi et al. \(2016\)](#) developed a model of the pairwise velocity PDFs which is valid for both dark matter particles and halos. The model requires the knowledge of the first three moments of the line-of-sight pairwise velocity distribution plus two well-defined dimensionless parameters, and each is a function of r, M_1, M_2 and z . [Kuruvilla & Porciani \(2018\)](#) found that a mixture of Gaussian PDFs can provide an excellent fit to the pairwise velocity PDFs for the line-of-sight component in the simulations. This model requires five functions to set full properties of the velocity PDFs. These five functions are dependent on r_p, r_π, M_1, M_2 and z for dark matter halos. Recently, [Cuesta-Lazaro et al. \(2020\)](#) proposed that a one-dimensional skewed-t PDF can provide a sufficient fit to the PDFs of the line-of-sight pairwise velocity for dark matter halos with $M \geq 10^{13} h^{-1} M_\odot$ at $z = 0$. A skewed-t PDF has four free parameters and each will depend on r_p, r_π, M_1, M_2 and z in general. Most previous studies have not studied the dependence of their PDF model on halo masses, redshifts, and the separation lengths. Future studies should focus on efficient calibrations and emulations of the mass-redshift-scale dependence of pairwise velocity PDFs for dark matter halos.

7. DISCUSSION AND CONCLUSION

In this paper, we developed a semi-analytic model of the pairwise velocity distributions of dark matter halos. The model is motivated by the findings and framework in [Tinker \(2007\)](#) and we re-calibrated the model parameters in the relation between the pairwise velocity and an environmental density around halo pairs using high-resolution N -body simulation covering a volume of $\sim 1 \text{ Gpc}^3$.

Our model has three functions related to the halo formation and the dependence of velocity dispersions on the cosmic mass density. By combining the log-normal PDF of cosmic mass density, our model can realize a significant non-Gaussianity in the pairwise velocity PDF with three parameters alone, while previous non-Gaussian PDF models require more parameters. We calibrated these three as a function of halo masses (M_1 and M_2), redshifts z and the separation lengths r using halo catalogs for $10^{12.5} < [h^{-1} M_\odot] < 10^{15}$ and $0 < z < 1$. We found that our

model can reproduce the first three non-zero velocity moments at $5 < r [h^{-1}\text{Mpc}] < 40$ for the halo masses of $10^{12.5} \lesssim M [h^{-1}M_{\odot}] \lesssim 10^{13.5}$ at $0.3 < z < 1$ with a 5%-level precision. For more massive halos or lower redshifts, we expect that our model is still able to explain the mean and dispersions of the pairwise velocity with a precision level of 10-20%. Based on the streaming model of two-point correlation functions, we also validated if our model can provide an accurate mapping of the two-point correlations between real and redshift space. For the mass-limited sample with $M \geq 10^{13.5} h^{-1}M_{\odot}$ at $z = 0.55$, we confirmed that our model can explain the redshift-space clustering monopole and quadropole in the range of $5 - 40$ and $10 - 30 h^{-1}\text{Mpc}$ within a 5%-level precision. This is valid even for a realistic SDSS-III BOSS CMASS galaxy sample based on the framework of a halo occupation distribution (HOD), if we have an accurate model of the real-space correlation function of galaxies. We then studied the dependence of the clustering multipoles on the velocity biases in the galaxy streaming motion by using our model. We found that a 20%-level bias in the mean and dispersion of the pairwise velocity of galaxies can induce a characteristic scale dependence of the observables at $\sim 10 \text{Mpc}$. It would be difficult to reproduce these features by varying the typical halo mass of galaxies alone, but more investigations are needed to make a robust conclusion.

Although our model of the pairwise velocity PDFs will play an important role in cosmological analyses in redshift surveys of massive galaxies, we require further improvements of the model before applying it to real data sets. In fact, the statistical uncertainties of the redshift-space clustering monopole and quadropole for the massive galaxies in BOSS already reach a level of a few percent at $1 - 10 h^{-1}\text{Mpc}$ (e.g. Reid et al. 2014) and our model precision is comparable to them at best. To improve the model precision, we may require a more sophisticated approach to calibrate model parameters such as Gaussian Process Regression, or some modifications in the functional forms in our model. Analyses involved with N -body particle data would be a key to improve our model, because the relationship between the cosmic mass density and the halo velocity is the essential part in our model. In addition, our model assumes the specific cosmological model in a ΛCDM scenario. We require further investigations to study the cosmological dependence of our model as well as extend our framework to include modified gravity theories. Upcoming redshift surveys aim at measuring the redshift-space clustering of galaxies with lower masses and higher redshifts than the mass- and redshift ranges explored in this study. It is thus important to extend our approach so as to be applicable for a wider range of halo masses and redshifts.

The model presented in this paper is an important first step toward statistical inference of the kinematics of galaxies from their clustering information in redshift surveys as well as interpretation of the small-scale measurements of the kinematic Sunyaev-Zel'dovich effect. Precise analyses with current and upcoming redshift surveys enable us to study the motion of several tracers of large-scale structures. The kinematic information of the tracers can provide an independent and important test of the standard cosmological model and allow us to examine possible deviations from General Relativity, if we have an accurate model of the pairwise velocity PDFs of dark matter halos. Our future work with the model of the pairwise velocity include a joint analysis of galaxy-galaxy lensing and the redshift-space clustering to infer the streaming motion of dark matter halos and investigation of the small-scale information in the kinematic Sunyaev-Zel'dovich effect on massive galaxies at various redshifts.

ACKNOWLEDGMENTS

We thank the $\nu^2\text{GC}$ collaboration for making their simulation data publicly available. This work is in part supported by MEXT KAKENHI Grant Number (18H04358, 19K14767). MS is supported by JSPS overseas Research Fellowships during his stay at the Jet Propulsion Laboratory (JPL). Numerical computations were in part carried out on Cray XC50 at Center for Computational Astrophysics, National Astronomical Observatory of Japan. EH, KM, and JR were supported by JPL, which is run by Caltech under a contract with the National Aeronautics and Space Administration (80NM0018D0004).

APPENDIX

A. LIST OF MODEL PARAMETERS

In this appendix, we provide the fitting functions in our model of the pairwise velocity distribution. The model is summarized in Section 2 and we introduce 58 parameters to explain the dependence of our model on halo masses, redshifts, separation lengths between halos.

For Eq. (22), we find the following forms provide a reasonable fit to the simulation results:

$$\mathcal{A}_\rho(M_1, M_2, z) = \frac{a_1(z)[D(z)a_2(z)y]^{a_3(z)}}{1 + [D(z)a_2(z)y]^{a_3(z)}}, \quad (\text{A1})$$

$$a_1(z) = 0.0385(1+z)^{-6.47} + 1.04, \quad (\text{A2})$$

$$a_2(z) = 0.488z^{3.21} + 0.737, \quad (\text{A3})$$

$$a_3(z) = -0.710(z - 0.310)^2 + 5.93, \quad (\text{A4})$$

$$y \equiv b_L(M_1, z) + b_L(M_2, z), \quad (\text{A5})$$

$$\mathcal{B}_\rho(M_1, M_2, z) = (26.7z^2 + 2.83z + 17.4) \left(\frac{M_1 + M_2}{10^{13} h^{-1} M_\odot} \right)^{0.631}, \quad (\text{A6})$$

$$\mathcal{C}_\rho(M_1, M_2, z) = - [0.109(z - 0.189)^2 + 0.862] \left(\frac{M_1 + M_2}{10^{13} h^{-1} M_\odot} \right)^{[-0.0223(z - 0.438)^2 + 0.204]}, \quad (\text{A7})$$

where $D(z)$ is the linear growth factor normalized to unity at $z = 0$, and $b_L(M, z)$ is the linear halo bias.

For Eq. (24), we adopt the following forms of

$$\mathcal{C}_t^{(0)}(M_1, M_2, z) = [-47.36(z - 0.54)^2 + 60.6] (R_{200b,0})^{0.701z^2 - 1.42z + 1.80}, \quad (\text{A8})$$

$$\mathcal{C}_t^{(1)}(M_1, M_2, z) = [-8.36(z - 0.572)^2 + 7.72] (R_{200b,0})^{0.0828z^2 - 0.509z + 0.042}, \quad (\text{A9})$$

$$\mathcal{C}_t^{(2)}(M_1, M_2, z) = 0.45, \quad (\text{A10})$$

$$p_t(M_1, M_2, z) = [0.866(z - 0.715)^2 - 2.16] (R_{200b,0})^{0.333(1+z)^{-4.82} - 0.0943}, \quad (\text{A11})$$

$$q_t(M_1, M_2, z) = -0.9, \quad (\text{A12})$$

$$\mathcal{C}_r^{(0)}(M_1, M_2, z) = [786.0z^2 - 2945z + 2970] \exp \left[- \left(\frac{0.248z^2 - 1.06z + 1.31}{R_{200b,0}} \right)^2 \right] R_{200b,\text{larger}}^2, \quad (\text{A13})$$

$$\mathcal{C}_r^{(1)}(M_1, M_2, z) = [-4.84z^2 + 0.431z + 26.4] (R_{200b,0})^{-0.0482z^2 - 0.103z + 0.484}, \quad (\text{A14})$$

$$\mathcal{C}_r^{(2)}(M_1, M_2, z) = [-0.109(z - 0.66)^2 + 0.497] (R_{200b,0})^{-0.161 - 0.0363z}, \quad (\text{A15})$$

$$p_r(M_1, M_2, z) = -4.0, \quad (\text{A16})$$

$$q_r(M_1, M_2, z) = -1.3, \quad (\text{A17})$$

where $R_{200b,0} = R_{200b}(M_1) + R_{200b}(M_2)$ and $R_{200b,\text{larger}} = \text{MAX}(R_{200b}(M_1), R_{200b}(M_2))$. The radii $R_{200b,0}$ and $R_{200b,\text{larger}}$ are in the unit of comoving h^{-1} Mpc.

B. HALO-BASED STREAMING MODEL OF REDSHIFT-SPACE CLUSTERING WITH A HALO OCCUPATION DISTRIBUTION

In this appendix, we briefly summarize an analytic expression of the redshift-space two point correlation with our model of the pairwise velocity distribution of dark matter halos for a given halo occupation distribution (HOD) (also see Tinker 2007, for more details). Note that we omit the redshift z for most parts in the following discussion for simplicity.

B.1. Setup

For a galaxy sample of interest, we assume that the galaxies can be decomposed into two types, centrals and satellites. For the central galaxies, we assume that they reside in the center of their host dark matter halos and individual host halos can have single central galaxies at most. For the satellite galaxies, we populate satellite galaxies to a halo only when a central galaxy exists. The HOD represents the mean number of galaxies in host halos with mass M and it is

given by

$$\langle N_{\text{gal}} \rangle_M = \langle N_{\text{cen}} \rangle_M + \langle N_{\text{sat}} \rangle_M, \quad (\text{B18})$$

where $\langle N_{\text{cen}} \rangle_M$ and $\langle N_{\text{sat}} \rangle_M$ are the HODs for centrals and satellites, respectively. In the following, we assume that the conditional distribution of the number of central galaxies in a given halo follows the Bernoulli distribution (i.e., can take only zero or one) with mean of $\langle N_{\text{cen}} \rangle_M$. On the other hand, the conditional distribution of the number of satellites is set by the Poisson distribution with mean λ_M . In this setup, the HOD for satellites can be expressed as $\langle N_{\text{sat}} \rangle_M = \langle N_{\text{cen}} \rangle_M \lambda_M$. Once the HOD is specified, we can compute the mean number density of the galaxies as

$$\bar{n}_g = \int dM \frac{dn}{dM} (\langle N_{\text{cen}} \rangle_M + \langle N_{\text{sat}} \rangle_M), \quad (\text{B19})$$

where dn/dM is the halo mass function. In this paper, we adopt the model of halo mass functions in Tinker et al. (2008). When comparing simulation results, one can use the mass function directly measured from the simulation. Although this is a better choice, we still adopt the model in Tinker et al. (2008) in this paper. For a sanity check, we compared the halo mass function at $z = 0.55$ in the $\nu^2\text{GC}$ simulation with the prediction by Tinker et al. (2008). We found a 10%-level difference at $M = 10^{13-14} h^{-1} M_\odot$, which is the most relevant mass range to the CMASS HOD. Nevertheless, this 10%-level difference is less dependent on the halo mass. In the clustering, a constant multiplicative bias in the mass function does not affect the model prediction (see Appendix B.2). Hence, we expect that the halo mass function by Tinker et al. (2008) is sufficient in our analyses.

B.2. Two-point correlation function

Within the HOD framework, the two-point correlation function of galaxies can be decomposed into two parts known as one-halo and two-halo terms. The one-halo term represents the two-point correlation within single halos, while two-halo term arises from the clustering among neighboring halos. For a given HOD in Appendix B.1, the one-halo terms in redshift space can be expressed as (Tinker 2007),

$$\xi_{1\text{h}}^S(s_p, s_\pi) = \xi_{1\text{h}}^{S,\text{cs}}(s_p, s_\pi) + \xi_{1\text{h}}^{S,\text{ss}}(s_p, s_\pi), \quad (\text{B20})$$

$$\xi_{1\text{h}}^{S,\text{cs}}(s_p, s_\pi) = \frac{1}{2\pi\bar{n}_g^2} \int dM \frac{dn}{dM} \langle N_{\text{sat}} \rangle_M \int_{-\infty}^{\infty} \frac{H(z) dr_\pi}{(1+z)} \frac{F_{\text{cs}}(\sqrt{s_p^2 + r_\pi^2} | M)}{s_p^2 + r_\pi^2} \mathcal{P}_{\text{cs}} \left(v_z = \frac{H(z)(s_p - r_\pi)}{(1+z)} \mid M \right), \quad (\text{B21})$$

$$\xi_{1\text{h}}^{S,\text{ss}}(s_p, s_\pi) = \frac{1}{2\pi\bar{n}_g^2} \int dM \frac{dn}{dM} \frac{\langle N_{\text{cen}} \rangle_M \lambda_M^2}{2} \int_{-\infty}^{\infty} \frac{H(z) dr_\pi}{(1+z)} \frac{F_{\text{ss}}(\sqrt{s_p^2 + r_\pi^2} | M)}{s_p^2 + r_\pi^2} \mathcal{P}_{\text{ss}} \left(v_z = \frac{H(z)(s_p - r_\pi)}{(1+z)} \mid M \right) \quad (\text{B22})$$

where $F_{\text{cs}}(r|M)$ is the fraction of number of central-satellite pairs at the radius of r in a halo with M , $F_{\text{ss}}(r|M)$ is the fraction of number of satellite-satellite pairs, \mathcal{P}_{cs} and \mathcal{P}_{ss} are the PDF of the pairwise velocity along a line of sight for central-satellite and satellite-satellite pairs, respectively. Note that $\int dr F_{\text{cs}}(r|M) = \int dr F_{\text{ss}}(r|M) = 1$.

When assuming the velocity distribution within each halo as an isotropic, isothermal Gaussian distribution and the satellite galaxy velocity dispersion in a halo is set to the virial dispersion, one can find

$$\mathcal{P}_{\text{cs}}(v_z | M) = \mathcal{N}(v_z, 0, \sigma_{\text{vir},M}), \quad (\text{B23})$$

$$\mathcal{P}_{\text{ss}}(v_z | M) = \mathcal{N}(v_z, 0, \sqrt{2}\sigma_{\text{vir},M}), \quad (\text{B24})$$

where $\mathcal{N}(x, \mu, \sigma)$ is a Gaussian distribution of a random field x with mean μ and variance σ^2 , and $\sigma_{\text{vir},M}$ represents the virial dispersion in a halo with mass M .

In addition, it is commonly assumed that the number density profile of satellites follows the mass density profile of its host dark matter halos. When the mass density profile in a halo is described by the (truncated) NFW profile (Navarro et al. 1996), the fraction of number of galaxy pairs is given by

$$F_{\text{cs}}(r|M) = \frac{1}{f(c)} \frac{r}{(r + r_s)^2}, \quad (\text{B25})$$

$$F_{\text{ss}}(r|M) = \frac{r}{2f^2(c)r_s^2} \int_0^c dx_1 Q(x_1, r/r_s, c), \quad (\text{B26})$$

where c and r_s are the halo concentration and scaled radius for the NFW profile, $f(c) = \ln(1+c) - c/(1+c)$, and

$$Q(x_1, x, c) = \begin{cases} 0 & (|x - x_1| > c) \\ (1 + x_1)^{-2} [(1 + |x - x_1|)^{-1} - (1 + x + x_1)^{-1}] & (x + x_1 < c, |x - x_1| \leq c) \\ (1 + x_1)^{-2} [(1 + |x - x_1|)^{-1} - (1 + c)^{-1}] & (x + x_1 \geq c, |x - x_1| \leq c) \end{cases}. \quad (\text{B27})$$

The two-halo term is then modeled by

$$1 + \xi_{2\text{h}}^S(s_p, s_\pi) = \int_{-\infty}^{\infty} \frac{H(z) dr_\pi}{(1+z)} \mathcal{P}_{2\text{h,g}} \left(v_z = \frac{H(z)(s_\pi - r_\pi)}{(1+z)} \mid s_p, r_\pi \right) \left[1 + \xi_{2\text{h}}(\sqrt{s_p^2 + r_\pi^2}) \right], \quad (\text{B28})$$

where $\xi_{2\text{h}}(r)$ is the two-halo term of real-space correlation function, and $\mathcal{P}_{2\text{h,g}}$ is the pairwise velocity PDF of galaxies for two separated halos. We here suppose that $\xi_{2\text{h}}(r)$ is accurately predicted by some approach such as perturbation-theory-based models (e.g. Desjacques et al. 2018, for a recent review), semi-analytic models (e.g. Hamana et al. 2001; Tinker et al. 2005; van den Bosch et al. 2013), and simulation-based models (e.g. Kwan et al. 2015; Nishimichi et al. 2019; Zhai et al. 2019). For the pairwise velocity PDF, we first compute the pairwise velocity PDF of dark matter halos for the line-of-sight component by using Eq. (7):

$$\begin{aligned} \mathcal{P}(v_z \mid r_p, r_\pi, M_1, M_2) &= \int dv_t \mathcal{P}(v_r, v_t \mid r, M_1, M_2) \delta_D \left(v_t - \frac{v_r \cos \theta - v_z}{\sin \theta} \right) \\ &= \int d\delta \mathcal{N} \left(v_z, \mu_r[\delta] \cos \theta, \sqrt{\Sigma_r^2[\delta] \cos^2 \theta + \Sigma_t^2[\delta] \sin^2 \theta} \right) \mathcal{F}(\delta \mid r, M_1, M_2), \end{aligned} \quad (\text{B29})$$

where $r = \sqrt{r_p^2 + r_\pi^2}$, $\cos \theta = r_\pi/r$, \mathcal{F} is the conditional PDF of cosmic mass density having a halo pair with masses of M_1 and M_2 within r , μ_r is the mean radial velocity at a given environmental density δ , and $\Sigma_{t,r}$ represents the velocity dispersion at a given δ . The details of these functions are found in Section 2 and Appendix A. We then incorporate Eq. (B29) with the HOD framework by assuming the Gaussian velocity distribution of satellites with the virial dispersion of σ_{vir} . The final expression of $\mathcal{P}_{2\text{h,g}}$ is given by

$$\begin{aligned} \mathcal{P}_{2\text{h,g}}(v_z \mid r_p, r_\pi) &= (n'_g)^{-2} \int_{M_{\text{min},0}}^{M_{\text{lim},1}} dM_1 \frac{dn}{dM_1} \langle N_{\text{gal}} \rangle_{M_1} \int_{M_{\text{min},0}}^{M_{\text{lim},2}} dM_2 \frac{dn}{dM_2} \langle N_{\text{gal}} \rangle_{M_2} \\ &\quad \times \mathcal{P}_{\text{g+h}}(v_z \mid r_p, r_\pi, M_1, M_2), \end{aligned} \quad (\text{B30})$$

$$\mathcal{P}_{\text{g+h}}(v_z \mid r_p, r_\pi, M_1, M_2) = \int d\delta \sum_{i=1}^4 w_i \mathcal{N}(v_z, \mu_r \cos \theta, \sigma_i) \mathcal{F}(\delta \mid r, M_1, M_2), \quad (\text{B31})$$

$$(n'_g)^2 = \int_{M_{\text{min},0}}^{M_{\text{lim},1}} dM_1 \frac{dn}{dM_1} \langle N_{\text{gal}} \rangle_{M_1} \int_{M_{\text{min},0}}^{M_{\text{lim},2}} dM_2 \frac{dn}{dM_2} \langle N_{\text{gal}} \rangle_{M_2}, \quad (\text{B32})$$

where $M_{\text{min},0}$ is the minimum halo mass that can host a galaxy (usually set by a sufficient small value), and

$$w_1 = \frac{\langle N_{\text{cen}} \rangle_{M_1} \langle N_{\text{cen}} \rangle_{M_2}}{\langle N_{\text{gal}} \rangle_{M_1} \langle N_{\text{gal}} \rangle_{M_2}}, \quad w_2 = \frac{\langle N_{\text{cen}} \rangle_{M_1} \langle N_{\text{sat}} \rangle_{M_2}}{\langle N_{\text{gal}} \rangle_{M_1} \langle N_{\text{gal}} \rangle_{M_2}}, \quad w_3 = \frac{\langle N_{\text{sat}} \rangle_{M_1} \langle N_{\text{cen}} \rangle_{M_2}}{\langle N_{\text{gal}} \rangle_{M_1} \langle N_{\text{gal}} \rangle_{M_2}}, \quad w_4 = \frac{\langle N_{\text{sat}} \rangle_{M_1} \langle N_{\text{sat}} \rangle_{M_2}}{\langle N_{\text{gal}} \rangle_{M_1} \langle N_{\text{gal}} \rangle_{M_2}}, \quad (\text{B33})$$

$$\sigma_1^2 = \Sigma_r^2(\delta, r, M_1, M_2) \cos^2 \theta + \Sigma_t^2(\delta, r, M_1, M_2) \sin^2 \theta, \quad (\text{B34})$$

$$\sigma_2^2 = \sigma_1^2 + \sigma_{\text{vir},M_2}^2, \quad \sigma_3^2 = \sigma_1^2 + \sigma_{\text{vir},M_1}^2, \quad \sigma_4^2 = \sigma_1^2 + \sigma_{\text{vir},M_1}^2 + \sigma_{\text{vir},M_2}^2. \quad (\text{B35})$$

In Eqs. (B30) and (B32), we set the upper limits of the integral to $R_{200\text{b}}(M_{\text{lim},1}) = r - R_{200\text{b}}(M_{\text{min},0})$ and $R_{200\text{b}}(M_{\text{lim},2}) = r - R_{200\text{b}}(M_1)$ by taking into account the effect of halo exclusion.

C. PERFORMANCE EVALUATION OF OUR MODEL FOR PAIRWISE VELOCITY DISTRIBUTION OF DARK MATTER HALOS

In this appendix, we evaluate our model precision for the profiles of the mean and dispersion in the pairwise velocity of dark matter halos in a wide range of halo masses and redshifts. Figures 13-16 summarize the ratio of the velocity moments between the simulation results and our model predictions for different halo masses ($M_2 \geq M_1$) and redshifts.

In each figure, the three left panels show the results for $M_1 = 10^{12.5-13} h^{-1} M_\odot$. From top to bottom, each panel shows the ratio of $\langle v_r \rangle$, σ_t , and σ_r , respectively. The three middle panels present the results for $M_1 = 10^{13-13.5} h^{-1} M_\odot$, while the three right panels are for $M_1 = 10^{13.5-14} h^{-1} M_\odot$. Figures 13, 14, 15, and 16 provide the results at $z = 0$, 0.30, 0.55, and 1.01, respectively. There are 10-20%-level differences for halo masses greater than $\sim 10^{13.5} h^{-1} M_\odot$, but our model can reproduce the simulation results for $10^{12.5} < M [h^{-1} M_\odot] < 10^{13.5}$ at $0.3 \lesssim z < 1$ with a 5%-level precision. We thus expect that our model would be suitable for analyses of massive-galaxy-sized dark matter halos at $z < 1$ targeted in various redshift surveys.

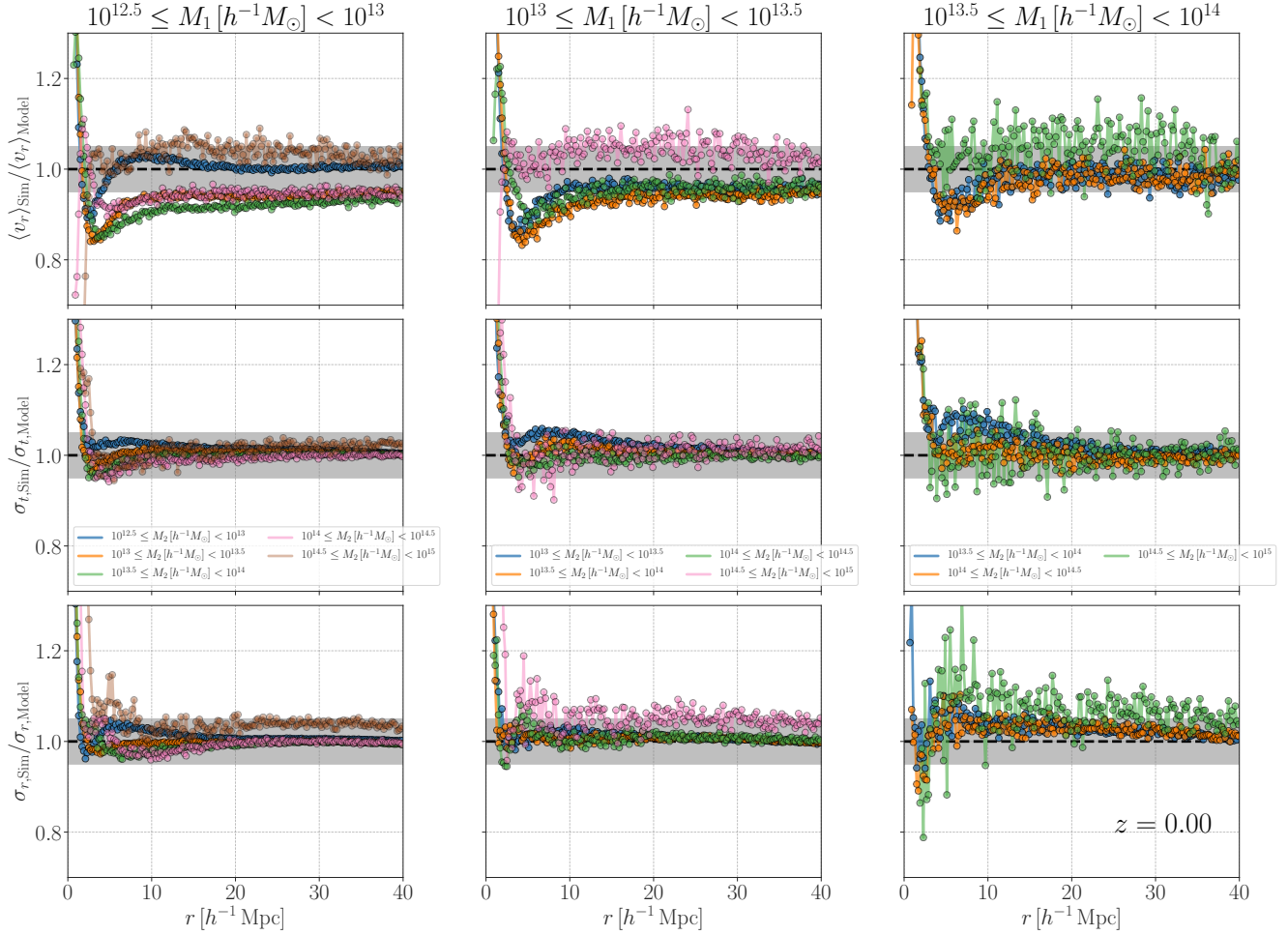


Figure 13. The mean and dispersion of pairwise-velocity of dark matter halos with various masses at the redshift of $z = 0$. Each panel shows the ratio of the velocity-moment profiles for different halo masses. The three left panels show the ratio of $\langle v_r \rangle$, σ_t , and σ_r for the halo masses of $M_1 = 10^{12.5-13} h^{-1} M_\odot$ and $M_2 \geq M_1$ from top to bottom. The middle and right panels represent the results for $M_1 = 10^{13-13.5} h^{-1} M_\odot$ and $M_1 = 10^{13.5-14} h^{-1} M_\odot$, respectively. For a reference, the gray filled region in each panel shows $\pm 5\%$ -level differences.

REFERENCES

- Behroozi, P. S., Wechsler, R. H., & Wu, H.-Y. 2013, *ApJ*,
 Bianchi, D., Percival, W. J., & Bel, J. 2016, *MNRAS*, 463,
 762, 109, doi: [10.1088/0004-637X/762/2/109](https://doi.org/10.1088/0004-637X/762/2/109)
 3783, doi: [10.1093/mnras/stw2243](https://doi.org/10.1093/mnras/stw2243)

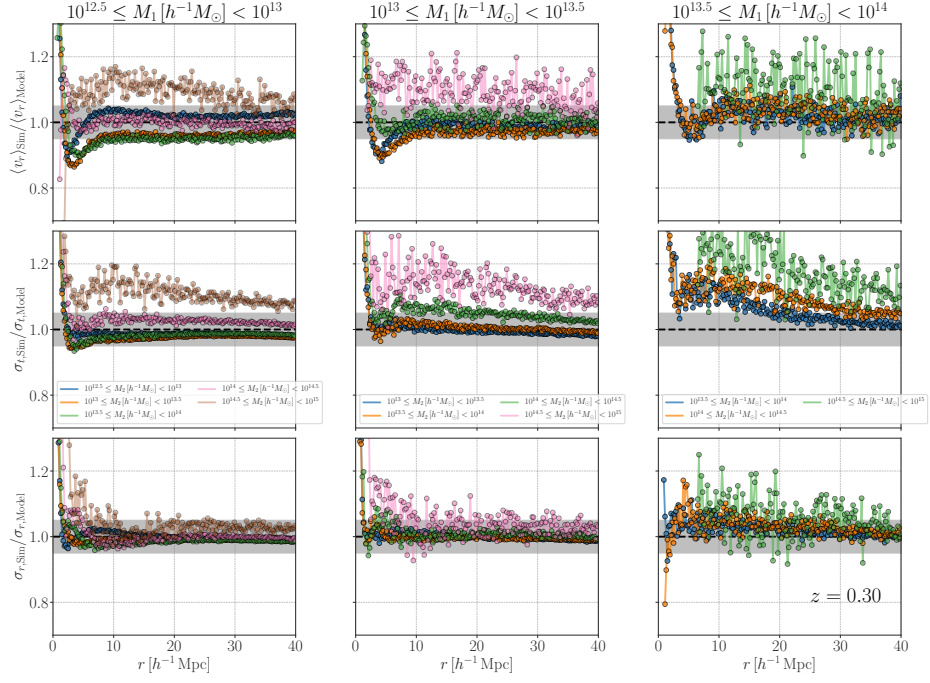


Figure 14. Similar to Figure 13, but this figure presents the results at the redshift of $z = 0.30$.

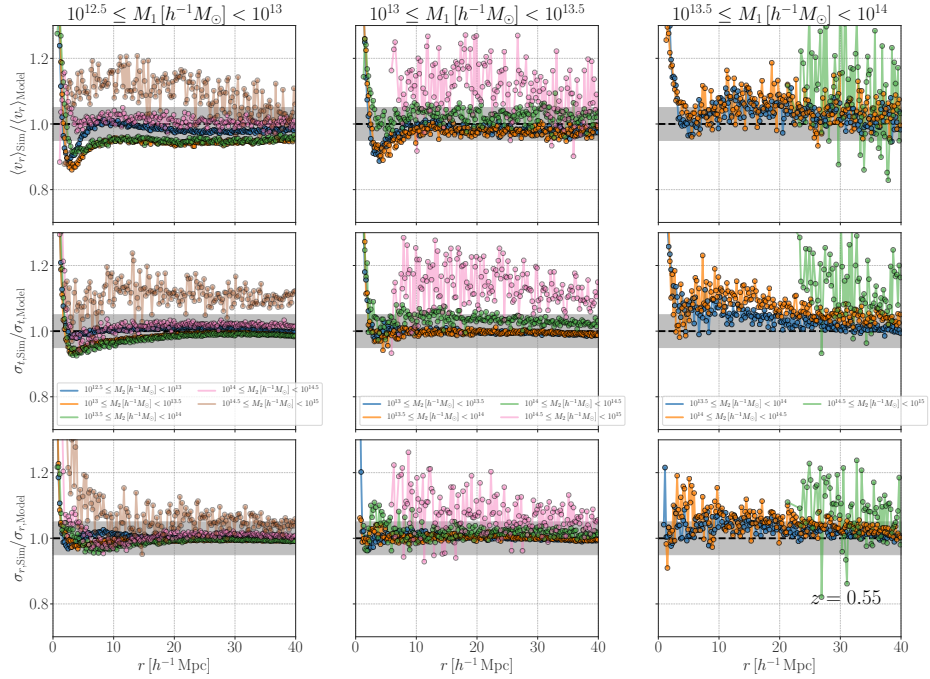


Figure 15. Similar to Figure 13, but this figure presents the results at the redshift of $z = 0.55$.

Bond, J. R., & Myers, S. T. 1996, ApJS, 103, 1,

doi: [10.1086/192267](https://doi.org/10.1086/192267)

Coles, P., & Jones, B. 1991, MNRAS, 248, 1,

doi: [10.1093/mnras/248.1.1](https://doi.org/10.1093/mnras/248.1.1)

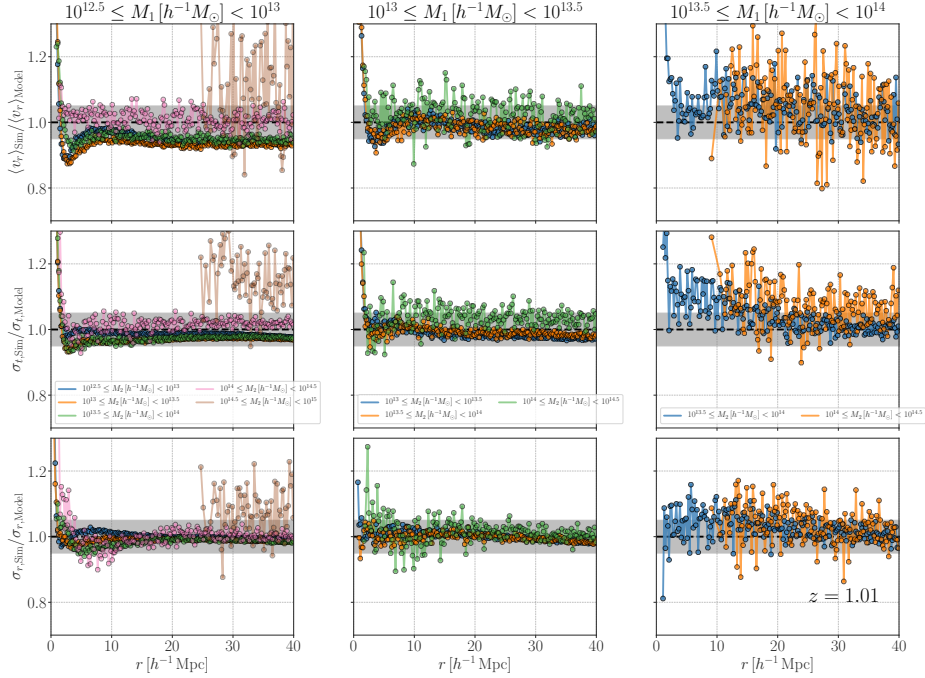


Figure 16. Similar to Figure 13, but this figure presents the results at the redshift of $z = 1.01$.

- Cooray, A. 2006, MNRAS, 365, 842, doi: [10.1111/j.1365-2966.2005.09747.x](https://doi.org/10.1111/j.1365-2966.2005.09747.x)
- Cooray, A., & Sheth, R. 2002, PhR, 372, 1, doi: [10.1016/S0370-1573\(02\)00276-4](https://doi.org/10.1016/S0370-1573(02)00276-4)
- Crocce, M., Pueblas, S., & Scoccimarro, R. 2006, MNRAS, 373, 369, doi: [10.1111/j.1365-2966.2006.11040.x](https://doi.org/10.1111/j.1365-2966.2006.11040.x)
- Croton, D. J., Gao, L., & White, S. D. M. 2007, MNRAS, 374, 1303, doi: [10.1111/j.1365-2966.2006.11230.x](https://doi.org/10.1111/j.1365-2966.2006.11230.x)
- Cuesta-Lazaro, C., Li, B., Eggemeier, A., et al. 2020, arXiv e-prints, arXiv:2002.02683, <https://arxiv.org/abs/2002.02683>
- De Bernardis, F., Aiola, S., Vavagiakis, E. M., et al. 2017, JCAP, 2017, 008, doi: [10.1088/1475-7516/2017/03/008](https://doi.org/10.1088/1475-7516/2017/03/008)
- Desjacques, V., Jeong, D., & Schmidt, F. 2018, PhR, 733, 1, doi: [10.1016/j.physrep.2017.12.002](https://doi.org/10.1016/j.physrep.2017.12.002)
- Diemer, B., & Kravtsov, A. V. 2015, ApJ, 799, 108, doi: [10.1088/0004-637X/799/1/108](https://doi.org/10.1088/0004-637X/799/1/108)
- Eisenstein, D. J., & Hu, W. 1998, ApJ, 496, 605, doi: [10.1086/305424](https://doi.org/10.1086/305424)
- Guo, H., Zheng, Z., Zehavi, I., et al. 2015, MNRAS, 446, 578, doi: [10.1093/mnras/stu2120](https://doi.org/10.1093/mnras/stu2120)
- Habib, S., Heitmann, K., Higdon, D., Nakhleh, C., & Williams, B. 2007, PhRvD, 76, 083503, doi: [10.1103/PhysRevD.76.083503](https://doi.org/10.1103/PhysRevD.76.083503)
- Hadzhiyska, B., Bose, S., Eisenstein, D., Hernquist, L., & Spergel, D. N. 2020, MNRAS, 493, 5506, doi: [10.1093/mnras/staa623](https://doi.org/10.1093/mnras/staa623)
- Hamana, T., Yoshida, N., Suto, Y., & Evrard, A. E. 2001, ApJL, 561, L143, doi: [10.1086/324677](https://doi.org/10.1086/324677)
- Hand, N., Addison, G. E., Aubourg, E., et al. 2012, PhRvL, 109, 041101, doi: [10.1103/PhysRevLett.109.041101](https://doi.org/10.1103/PhysRevLett.109.041101)
- Hearin, A. P. 2015, MNRAS, 451, L45, doi: [10.1093/mnras/slv064](https://doi.org/10.1093/mnras/slv064)
- Hellwing, W. A., Barreira, A., Frenk, C. S., Li, B., & Cole, S. 2014, PhRvL, 112, 221102, doi: [10.1103/PhysRevLett.112.221102](https://doi.org/10.1103/PhysRevLett.112.221102)
- Ishiyama, T., Enoki, M., Kobayashi, M. A. R., et al. 2015, PASJ, 67, 61, doi: [10.1093/pasj/psv021](https://doi.org/10.1093/pasj/psv021)
- Ishiyama, T., Fukushige, T., & Makino, J. 2009, PASJ, 61, 1319, doi: [10.1093/pasj/61.6.1319](https://doi.org/10.1093/pasj/61.6.1319)
- Ishiyama, T., Nitadori, K., & Makino, J. 2012, arXiv e-prints, arXiv:1211.4406, <https://arxiv.org/abs/1211.4406>
- Jain, B., & Zhang, P. 2008, PhRvD, 78, 063503, doi: [10.1103/PhysRevD.78.063503](https://doi.org/10.1103/PhysRevD.78.063503)
- Kayo, I., Taruya, A., & Suto, Y. 2001, ApJ, 561, 22, doi: [10.1086/323227](https://doi.org/10.1086/323227)
- Kofman, L., Bertschinger, E., Gelb, J. M., Nusser, A., & Dekel, A. 1994, ApJ, 420, 44, doi: [10.1086/173541](https://doi.org/10.1086/173541)
- Komatsu, E., Dunkley, J., Nolta, M. R., et al. 2009, ApJS, 180, 330, doi: [10.1088/0067-0049/180/2/330](https://doi.org/10.1088/0067-0049/180/2/330)
- Kuruvilla, J., & Porciani, C. 2018, MNRAS, 479, 2256, doi: [10.1093/mnras/sty1654](https://doi.org/10.1093/mnras/sty1654)

- Kwan, J., Bhattacharya, S., Heitmann, K., & Habib, S. 2013, *ApJ*, 768, 123, doi: [10.1088/0004-637X/768/2/123](https://doi.org/10.1088/0004-637X/768/2/123)
- Kwan, J., Heitmann, K., Habib, S., et al. 2015, *ApJ*, 810, 35, doi: [10.1088/0004-637X/810/1/35](https://doi.org/10.1088/0004-637X/810/1/35)
- Lam, T. Y., Nishimichi, T., Schmidt, F., & Takada, M. 2012, *PhRvL*, 109, 051301, doi: [10.1103/PhysRevLett.109.051301](https://doi.org/10.1103/PhysRevLett.109.051301)
- Lam, T. Y., & Sheth, R. K. 2008, *MNRAS*, 389, 1249, doi: [10.1111/j.1365-2966.2008.13621.x](https://doi.org/10.1111/j.1365-2966.2008.13621.x)
- Landy, S. D., & Szalay, A. S. 1993, *ApJ*, 412, 64, doi: [10.1086/172900](https://doi.org/10.1086/172900)
- Lawrence, E., Heitmann, K., White, M., et al. 2010, *ApJ*, 713, 1322, doi: [10.1088/0004-637X/713/2/1322](https://doi.org/10.1088/0004-637X/713/2/1322)
- Leauthaud, A., Tinker, J., Bundy, K., et al. 2012, *ApJ*, 744, 159, doi: [10.1088/0004-637X/744/2/159](https://doi.org/10.1088/0004-637X/744/2/159)
- Lewis, A., Challinor, A., & Lasenby, A. 2000, *ApJ*, 538, 473, doi: [10.1086/309179](https://doi.org/10.1086/309179)
- Li, B., & Efstathiou, G. 2012, *MNRAS*, 421, 1431, doi: [10.1111/j.1365-2966.2011.20404.x](https://doi.org/10.1111/j.1365-2966.2011.20404.x)
- Masters, K. L., Maraston, C., Nichol, R. C., et al. 2011, *MNRAS*, 418, 1055, doi: [10.1111/j.1365-2966.2011.19557.x](https://doi.org/10.1111/j.1365-2966.2011.19557.x)
- McClintock, T., Rozo, E., Becker, M. R., et al. 2019, *ApJ*, 872, 53, doi: [10.3847/1538-4357/aaf568](https://doi.org/10.3847/1538-4357/aaf568)
- More, S., Miyatake, H., Mandelbaum, R., et al. 2015, *ApJ*, 806, 2, doi: [10.1088/0004-637X/806/1/2](https://doi.org/10.1088/0004-637X/806/1/2)
- Navarro, J. F., Frenk, C. S., & White, S. D. M. 1996, *ApJ*, 462, 563, doi: [10.1086/177173](https://doi.org/10.1086/177173)
- Nishimichi, T., Takada, M., Takahashi, R., et al. 2019, *ApJ*, 884, 29, doi: [10.3847/1538-4357/ab3719](https://doi.org/10.3847/1538-4357/ab3719)
- Padilla, N., Contreras, S., Zehavi, I., Baugh, C. M., & Norberg, P. 2019, *MNRAS*, 486, 582, doi: [10.1093/mnras/stz824](https://doi.org/10.1093/mnras/stz824)
- Peebles, P. J. E. 1980, *The large-scale structure of the universe*
- Planck Collaboration, Ade, P. A. R., Aghanim, N., et al. 2016, *A&A*, 594, A13, doi: [10.1051/0004-6361/201525830](https://doi.org/10.1051/0004-6361/201525830)
- Prada, F., Klypin, A. A., Cuesta, A. J., Betancort-Rijo, J. E., & Primack, J. 2012, *MNRAS*, 423, 3018, doi: [10.1111/j.1365-2966.2012.21007.x](https://doi.org/10.1111/j.1365-2966.2012.21007.x)
- Reid, B. A., Seo, H.-J., Leauthaud, A., Tinker, J. L., & White, M. 2014, *MNRAS*, 444, 476, doi: [10.1093/mnras/stu1391](https://doi.org/10.1093/mnras/stu1391)
- Reid, B. A., & Spergel, D. N. 2009, *ApJ*, 698, 143, doi: [10.1088/0004-637X/698/1/143](https://doi.org/10.1088/0004-637X/698/1/143)
- Soccimarro, R. 2004, *PhRvD*, 70, 083007, doi: [10.1103/PhysRevD.70.083007](https://doi.org/10.1103/PhysRevD.70.083007)
- Shen, J., Abel, T., Mo, H. J., & Sheth, R. K. 2006, *ApJ*, 645, 783, doi: [10.1086/504513](https://doi.org/10.1086/504513)
- Shin, J., Kim, J., Pichon, C., Jeong, D., & Park, C. 2017, *ApJ*, 843, 73, doi: [10.3847/1538-4357/aa74b9](https://doi.org/10.3847/1538-4357/aa74b9)
- Smith, K. M., Madhavacheril, M. S., Münchmeyer, M., et al. 2018, arXiv e-prints, arXiv:1810.13423, <https://arxiv.org/abs/1810.13423>
- Sugiyama, N. S., Okumura, T., & Spergel, D. N. 2017, *JCAP*, 2017, 057, doi: [10.1088/1475-7516/2017/01/057](https://doi.org/10.1088/1475-7516/2017/01/057)
- . 2018, *MNRAS*, 475, 3764, doi: [10.1093/mnras/stx3362](https://doi.org/10.1093/mnras/stx3362)
- Takahashi, R., Sato, M., Nishimichi, T., Taruya, A., & Oguri, M. 2012, *ApJ*, 761, 152, doi: [10.1088/0004-637X/761/2/152](https://doi.org/10.1088/0004-637X/761/2/152)
- Tinker, J., Kravtsov, A. V., Klypin, A., et al. 2008, *ApJ*, 688, 709, doi: [10.1086/591439](https://doi.org/10.1086/591439)
- Tinker, J. L. 2007, *MNRAS*, 374, 477, doi: [10.1111/j.1365-2966.2006.11157.x](https://doi.org/10.1111/j.1365-2966.2006.11157.x)
- Tinker, J. L., Robertson, B. E., Kravtsov, A. V., et al. 2010, *ApJ*, 724, 878, doi: [10.1088/0004-637X/724/2/878](https://doi.org/10.1088/0004-637X/724/2/878)
- Tinker, J. L., Weinberg, D. H., Zheng, Z., & Zehavi, I. 2005, *ApJ*, 631, 41, doi: [10.1086/432084](https://doi.org/10.1086/432084)
- Tinker, J. L., Brownstein, J. R., Guo, H., et al. 2017, *ApJ*, 839, 121, doi: [10.3847/1538-4357/aa6845](https://doi.org/10.3847/1538-4357/aa6845)
- van den Bosch, F. C., More, S., Cacciato, M., Mo, H., & Yang, X. 2013, *MNRAS*, 430, 725, doi: [10.1093/mnras/sts006](https://doi.org/10.1093/mnras/sts006)
- Weinberg, D. H., Mortonson, M. J., Eisenstein, D. J., et al. 2013, *PhR*, 530, 87, doi: [10.1016/j.physrep.2013.05.001](https://doi.org/10.1016/j.physrep.2013.05.001)
- White, M., Blanton, M., Bolton, A., et al. 2011, *ApJ*, 728, 126, doi: [10.1088/0004-637X/728/2/126](https://doi.org/10.1088/0004-637X/728/2/126)
- Xu, X., & Zheng, Z. 2018, *MNRAS*, 479, 1579, doi: [10.1093/mnras/sty1547](https://doi.org/10.1093/mnras/sty1547)
- Zehavi, I., Zheng, Z., Weinberg, D. H., et al. 2005, *ApJ*, 630, 1, doi: [10.1086/431891](https://doi.org/10.1086/431891)
- . 2011, *ApJ*, 736, 59, doi: [10.1088/0004-637X/736/1/59](https://doi.org/10.1088/0004-637X/736/1/59)
- Zentner, A. R., Hearin, A. P., & van den Bosch, F. C. 2014, *MNRAS*, 443, 3044, doi: [10.1093/mnras/stu1383](https://doi.org/10.1093/mnras/stu1383)
- Zhai, Z., Tinker, J. L., Becker, M. R., et al. 2019, *ApJ*, 874, 95, doi: [10.3847/1538-4357/ab0d7b](https://doi.org/10.3847/1538-4357/ab0d7b)
- Zheng, Z., Coil, A. L., & Zehavi, I. 2007, *ApJ*, 667, 760, doi: [10.1086/521074](https://doi.org/10.1086/521074)
- Zheng, Z., & Guo, H. 2016, *MNRAS*, 458, 4015, doi: [10.1093/mnras/stw523](https://doi.org/10.1093/mnras/stw523)
- Zheng, Z., Zehavi, I., Eisenstein, D. J., Weinberg, D. H., & Jing, Y. P. 2009, *ApJ*, 707, 554, doi: [10.1088/0004-637X/707/1/554](https://doi.org/10.1088/0004-637X/707/1/554)
- Zu, Y., & Weinberg, D. H. 2013, *MNRAS*, 431, 3319, doi: [10.1093/mnras/stt411](https://doi.org/10.1093/mnras/stt411)
- Zu, Y., Weinberg, D. H., Jennings, E., Li, B., & Wyman, M. 2014, *MNRAS*, 445, 1885, doi: [10.1093/mnras/stu1739](https://doi.org/10.1093/mnras/stu1739)